Commun. Comput. Phys.
doi: 10.4208/cicp.070312.061112a

Vol. **14**, No. 3, pp. 664-702
September 2013

Boundary Conditions for Limited Area Models Based on the Shallow Water Equations

Arthur Bousquet[1], Madalina Petcu[2,3], Ming-Cheng Shiue[1,4],
Roger Temam[1,*] and Joseph Tribbia[5]

[1] *The Institute for Scientific Computing and Applied Mathematics, Indiana University, Bloomington, IN 47405, USA.*
[2] *Laboratoire de Mathematiques et Applications, UMR 6086, Universite de Poitiers, France.*
[3] *The Institute of Mathematics of the Romanian Academy, Bucharest, Romania.*
[4] *Department of Applied Mathematics, National Chiao Tung University, Hsinchu, Taiwan.*
[5] *National Center for Atmospheric Research, Boulder, Colorado, USA.*

Received 7 March 2012; Accepted (in revised version) 6 November 2012

Communicated by Jie Shen

Abstract. A new set of boundary conditions has been derived by rigorous methods for the shallow water equations in a limited domain. The aim of this article is to present these boundary conditions and to report on numerical simulations which have been performed using these boundary conditions. The new boundary conditions which are mildly dissipative let the waves move freely inside and outside the domain. The problems considered include a one-dimensional shallow water system with two layers of fluids and a two-dimensional inviscid shallow water system in a rectangle.

AMS subject classifications: 35L04, 35Q35, 65M08, 65M55

Key words: Boundary conditions, finite volumes, shallow water.

1 Introduction

The problem of boundary conditions in a limited domain is recognized as an important problem in geophysical fluid dynamics. In its primary form, the problem which was

---

*Corresponding author. *Email addresses:* `arthbous@indiana.edu` (A. Bousquet), `madalina.petcu@math.univ-poitiers.fr` (M. Petcu), `mingcheng.shiue@gmail.com` (M. Shiue), `temam@indiana.edu` (R. Temam), `tribbia@ucar.edu` (J. Tribbia)

identified already by J. Von Neumann and J. Charney, is to choose the boundary conditions for a limited area model (LAM), when the boundary of the computational domain or part of it has no physical relevance and there are no physical laws prescribing a natural boundary condition. This old problem which persists in this form, reappears in other contemporary developments. For multi-level numerical methods, the issue of boundary conditions is present for each of the subdomains of the fine grids; see e.g. [24]. Also, in many attempts at modeling, this issue occurs as well, the usual remedy being to use the space periodic boundary conditions. However space periodicity can be physically unrealistic in particular because it generally implies conservation of energy; see e.g. [31] for the modeling of clouds where the lack of suitable boundary conditions prevents from studying the interactions of contiguous vertical columns.

Many authors have addressed the problem from different angles, but the approach is generally based on some form of physical intuition or on some modeling; see e.g. [5–7, 22, 24–26, 28, 32, 36, 37], the tutorial [38] and the references therein. In this article we would like to address this issue in the light of theoretical (mathematical) results connected to the study of the well-posedness of the initial and boundary value problems. The problems studied here are the two-layer shallow water equations, in space dimension one and the (one layer) shallow water equations in a rectangle in space dimension two; see [30] for the one-dimensional two-layer shallow water equations; see also [29] for the one-dimensional (one layer) shallow water equations; and see [8, 20, 21] for the general approach to initial and boundary value problems for hyperbolic equations based on the so-called Kreiss-Lopatinsky conditions; see also [23].

Beside presenting these boundary conditions, another aim of this article is to report on numerical tests performed using these conditions. One feature of these boundary conditions is that they are (mildly) dissipative, a property which is used of course in the theoretical study. In our numerical studies these boundary conditions appear to let the waves move freely inside or outside the domain. In the mathematical literature such boundary conditions are called "transparent" boundary conditions; see e.g. [11, 12, 14]. Note that our objective per se is not to derive transparent boundary conditions, but it happens that the boundary conditions coming from the existence and uniqueness theorem are transparent to a certain extent.

The first example on which we report in Section 2 is that of two layers of inviscid shallow water equations in space dimension one. Note that this case studied in [25] and from the mathematical perspective in [30] raises substantial new difficulties as compared to the case of one layer. Indeed this system may not be hyperbolic, see e.g. [3, 9, 25] and also [10,33,37] and as emphasized already in [27] the boundary conditions for multilayer shallow water equations can not be of local type, which means in the present case, that on each layer, the boundary conditions possibly involve the other layer(s). The boundary conditions that we discuss below are studied on the theoretical side in [30] and on the computational side they appear to be transparent to some extent.

The second case that we test and discuss in Section 3 is that of the inviscid shallow water equations in a rectangle in space dimension two. Note that here there is no supporting theory (so far) concerning the existence and uniqueness of solutions, because the domain, being a rectangle, is not smooth, and the available theoretical results only apply to flows in a smooth domain. However we surmise that the same type of procedure is applicable and we are working on it from the theoretical side, see [15–17]. Note that the boundary conditions that we implement and study numerically come from an heuristic application of the Kreiss-Lopatinsky theory. In this article, for this flow, we start from the Rossby equatorial soliton which is a classical test model in the literature as recalled below. The equations are the two-dimensional shallow water equations in a rectangle with special values of the coefficient and the initial data.The boundary conditions for the test problem are either the Dirichlet boundary conditions as in the original Rossby equatorial soliton (see below) or the Neumann boundary conditions as kindly suggested by a referee; both are not supported by any theoretical study. Everything else being unchanged, we replace the Dirichlet or Neumann boundary conditions by our "transparent" boundary conditions and our simulations show that the Rossby equatorial soliton with our proposed boundary conditions smoothly leaves the domain, confirming that these boundary conditions are indeed transparent in this case.

Our aim in this article is not to compare the theoretical rigorous boundary conditions with the many other open boundary conditions that are available in the literature, as we believe this would be a substantial work of doubtful interest. Nevertheless, for the two-dimensional equatorial Rossby soliton it was tempting to compare our boundary conditions with the Dirichlet and Neumann boundary conditions, the Dirichlet boundary conditions being, as we said, part of the equatorial Rossby soliton, a classical test which the referees asked us to perform in a previous computational article [1]. Our simulations show undesirable reflexions when the soliton reaches the boundary of the domain when using the Dirichlet or Neumann boundary conditions, unlike the proposed transparent conditions. Furthermore, for the Dirichlet boundary conditions the calculations blow up at some time, whereas for the Neumann boundary conditions substantial reflexions occur at the boundary but they are less significant than for the Dirichlet condition, and the soliton eventually leaves the domain of calculation.

Finally, we also discuss in each case some of the numerical techniques used to actually implement these boundary conditions. This is not straightforward and indeed several computational subtleties are necessary when implementing the boundary conditions, both for the boundary conditions themselves and for the equations. Further indications for related situations can be found in [1,34].

2 Two-layer shallow water equations

In this Section, we consider the two-layer shallow water equations for a flow along a simple channel as follows:

$$
\begin{cases}
\dfrac{\partial u_1}{\partial t}+u_1\dfrac{\partial u_1}{\partial x}=-g\dfrac{\partial}{\partial x}(h_1+h_2+B)+g'\dfrac{\partial h_2}{\partial x}, \\
\dfrac{\partial h_1}{\partial t}=-\dfrac{1}{b}\dfrac{\partial}{\partial x}(bu_1h_1), \\
\dfrac{\partial u_2}{\partial t}+u_2\dfrac{\partial u_2}{\partial x}=-g\dfrac{\partial}{\partial x}(h_1+h_2+B), \\
\dfrac{\partial h_2}{\partial t}=-\dfrac{1}{b}\dfrac{\partial}{\partial x}(bu_2h_2).
\end{cases}
\tag{2.1}
$$

Here, we assume that there are two distinct immiscible fluid layers, these layers being described by the velocities u_i that depend on the horizontal x-coordinates but independent on y and on the vertical position, the constant densities ρ_i, and the heights h_i with $i=1,2$. The channel has length L with a rectangular cross-section with variable width $b(x)$ and the bottom height $B(x)$ (see Fig. 1). The constant g' represents the reduced gravity which is defined as follows:

$$g'\equiv\frac{g(\rho_1-\rho_2)}{\rho_1},$$

where g is the gravitational acceleration.

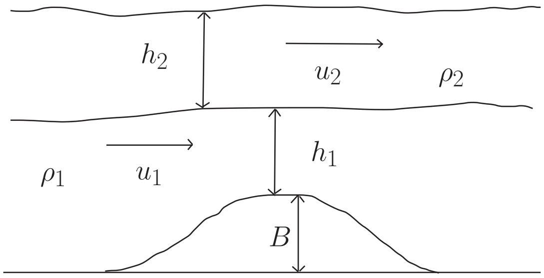

Figure 1: The two-layer shallow water model.

As explained in [2, 3], the difficulty with the two-layer shallow water equations is that the system (2.1) is not hyperbolic. In order to overcome the difficulty, we consider an approximation of this model available in the literature, see [25]; see also [2,4] for different ways in overcoming this difficulty. In [25], the authors remarked that the barotropic and baroclinic modes couple very weakly if $g'\ll g$ but these modes couple strongly in the presence of nonuniform topography near the boundary. In this article, we assume that the channel has straight walls ($b=1$) and the topography is added to render these examples physically more interesting. To avoid that these modes couple strongly at the open boundary, we assume that the bottom near the boundary is flat. Thus, we can then consider the two modes separately. As in [25], by defining

$$h=h_1+h_2, \qquad u=\frac{u_1h_1+u_2h_2}{h}, \tag{2.2}$$

the equations for the barotropic mode are derived by neglecting g' entirely and assuming that $u_1 \approx u_2$ so that we find:

$$\begin{cases} \dfrac{\partial u}{\partial t}+u\dfrac{\partial u}{\partial x}+g\dfrac{\partial h}{\partial x}=-g\dfrac{\partial B}{\partial x}, \\ \dfrac{\partial h}{\partial t}+\dfrac{\partial}{\partial x}(uh)=0. \end{cases} \tag{2.3}$$

Note that these equations (2.3) are the same as the single-layer shallow water equations. By writing $v=u_1-u_2$, the equations for the baroclinic mode read

$$\begin{cases} \dfrac{\partial v}{\partial t}+\dfrac{\partial}{\partial x}\Big(uv+\dfrac{(h-2h_1)v^2}{2h}+g'h_1\Big)=g'\dfrac{\partial h}{\partial x}, \\ \dfrac{\partial h_1}{\partial t}+\dfrac{\partial}{\partial x}\Big(uh_1+\dfrac{h_1(h-h_1)v}{h}\Big)=0. \end{cases} \tag{2.4}$$

Now, we will propose open boundary conditions for this approximate model (2.3)-(2.4). Indeed, we first consider the boundary conditions for the barotropic mode. We use the boundary conditions proposed in [25] and studied in [30] since the equations for the barotropic mode are exactly the equations for the single-layer shallow water equations. Thus, as in [30], for barotropically subcritical flows ($u^2 < gh$), boundary conditions are given as follows:

$$\begin{cases} \alpha_1(0,t):=u(0,t)+2\sqrt{gh(0,t)}=u_0+2\sqrt{gh_0}, \\ \beta_1(L,t):=u(L,t)-2\sqrt{gh(L,t)}=u_0-2\sqrt{gh_0}, \end{cases} \tag{2.5}$$

and for barotropically supercritical flows ($u^2 > gh$), boundary conditions are given as follows:

$$\begin{cases} \alpha_1(0,t):=u(0,t)+2\sqrt{gh(0,t)}=u_0+2\sqrt{gh_0}, \\ \beta_1(0,t):=u(0,t)-2\sqrt{gh(0,t)}=u_0-2\sqrt{gh_0}, \end{cases} \tag{2.6}$$

where u_0 and h_0 are constant reference states satisfying $u(0,t)=u(L,t)=u_0$ and $h(0,t)=h(L,t)=h_0$ at $t=0$.

For the baroclinic mode, as in [30], the flow is said to be baroclinically subcritical if

$$\Big(u+\frac{v(h-2h_1)}{h}\Big)^2<\frac{h_1(h-h_1)}{h^2}(g'h-v^2), \qquad \text{and} \qquad g'h-v^2>0,$$

where the left hand side in the first inequality is the square of the speed of interfacial long waves; the flow is said to be baroclinically supercritical if

$$\Big(u+\frac{v(h-2h_1)}{h}\Big)^2>\frac{h_1(h-h_1)}{h^2}(g'h-v^2), \qquad \text{and} \qquad g'h-v^2>0.$$

Note that when the flow is barotropically supercritical, it is also baroclinically supercritical.

As in [30], we assume for simplicity that the reference barotropic state is the constant state $h=h_0$, $u=u_0$ with the same values as in the initial data, in (2.6). Then, for baroclinically subcritical flows, the boundary conditions are given as follows:

$$\begin{cases} \alpha_2(0,t):=\arcsin\Big(\dfrac{v(0,t)}{\sqrt{g'h(0,t)}}\Big)-\arcsin\Big(\dfrac{h(0,t)-2h_1(0,t)}{h(0,t)}\Big)=-\arcsin\Big(\dfrac{h_0-2h_{1,0}}{h_0}\Big), \\ \beta_2(L,t):=\arcsin\Big(\dfrac{v(L,t)}{\sqrt{g'h(L,t)}}\Big)+\arcsin\Big(\dfrac{h(L,t)-2h_1(L,t)}{h(L,t)}\Big)=\arcsin\Big(\dfrac{h_0-2h_{1,0}}{h_0}\Big); \end{cases} \tag{2.7}$$

while for baroclinically supercritical flows, the boundary conditions are given as follows:

$$\begin{cases} \alpha_2(0,t):=\arcsin\Big(\dfrac{v(0,t)}{\sqrt{g'h(0,t)}}\Big)-\arcsin\Big(\dfrac{h(0,t)-2h_1(0,t)}{h(0,t)}\Big)=-\arcsin\Big(\dfrac{h_0-2h_{1,0}}{h_0}\Big), \\ \beta_2(0,t):=\arcsin\Big(\dfrac{v(0,t)}{\sqrt{g'h(0,t)}}\Big)+\arcsin\Big(\dfrac{h(0,t)-2h_1(0,t)}{h(0,t)}\Big)=\arcsin\Big(\dfrac{h_0-2h_{1,0}}{h_0}\Big), \end{cases} \tag{2.8}$$

where $h_{1,0}$ is the constant reference state.

Remark 2.1. Note that we might consider the right-hand sides of (2.5)-(2.8) to be time-dependent as in [29,30]. As remarked in [25], the physical meaning is clear if the right-hand sides of (2.5)-(2.8) are time-independent. In these cases, the flow becomes steady-state after the waves generated by the initial perturbation move out of the domain.

2.1 Numerical algorithms

As in [34], a generalization of the semi-discrete central-upwind method is applied for solving the approximate model (2.3)-(2.4) supplemented with the proposed boundary conditions (2.5)-(2.8). For the spatial discretization, the semi-discrete central-upwind method in [18,19] is applied with suitable boundary treatment procedures. Our numerical approach is to solve (2.3)-(2.4) for points inside the domain in a first step and then to update the boundary values based on the numerical data from the first step. Following the method in [34], we rewrite Eq. (2.3) for the barotropic flow and Eq. (2.4) for the baroclinic flow in the conservative form

$$\frac{\partial}{\partial t}U+\frac{\partial}{\partial x}F(U)=S(U,t,x), \quad (x,t)\in[0,L]\times[0,T], \tag{2.9}$$

where L is the length of the physical domain, T is the computation time and

$$U=\begin{pmatrix} uh \\ h \\ v \\ h_1 \end{pmatrix}, \quad F=\begin{pmatrix} hu^2+\frac{1}{2}gh^2 \\ uh \\ uv+\frac{(h-2h_1)v^2}{2h}+g'h_1-g'h \\ uh_1+\frac{h_1(h-h_1)v}{h} \end{pmatrix}, \quad S=\begin{pmatrix} -gh\frac{\partial B}{\partial x} \\ 0 \\ 0 \\ 0 \end{pmatrix}.$$

We consider a uniform spatial grid $x_j=(j-1)\Delta x$, $j=1,\cdots,M+1$, where M is the number of grid points and $\Delta x=L/M$ and denote by $\bar{U}_j(t)$ the cell average of $U(t,\cdot)$ over the j-cell $I_j=(x_{j-\frac{1}{2}},x_{j+\frac{1}{2}})$, that is

$$\bar{U}_j(t):=\frac{1}{\Delta x}\int_{x_{j-\frac{1}{2}}}^{x_{j+\frac{1}{2}}}U(t,x)dx. \tag{2.10}$$

Integrating Eq. (2.10) over the j-cell I_j, the resulting equation reads

$$\frac{d}{dt}\bar{U}_j(t)+\frac{F(U(t,x_{j+\frac{1}{2}}))-F(U(t,x_{j-\frac{1}{2}}))}{\Delta x}=\frac{1}{\Delta x}\int_{x_{j-\frac{1}{2}}}^{x_{j+\frac{1}{2}}}S(U(t,x),t,x)dx. \tag{2.11}$$

The approximations of the function $F(U)$ at the points $x=x_{j\pm\frac{1}{2}}$ are given writing (see [18,19]):

$$F(U(t,x_{j+\frac{1}{2}}))\approx F_{j+\frac{1}{2}}(t), \tag{2.12}$$

where

$$F_{j+\frac{1}{2}}(t):=\frac{a^+_{j+\frac{1}{2}}F(U^-_{j+\frac{1}{2}})-a^-_{j+\frac{1}{2}}F(U^+_{j+\frac{1}{2}})}{a^+_{j+\frac{1}{2}}-a^-_{j+\frac{1}{2}}}+\frac{a^+_{j+\frac{1}{2}}a^-_{j+\frac{1}{2}}}{a^+_{j+\frac{1}{2}}-a^-_{j+\frac{1}{2}}}[U^+_{j+\frac{1}{2}}-U^-_{j+\frac{1}{2}}]. \tag{2.13}$$

Here, $U^+_{j+\frac{1}{2}}:=p_{j+1}(t,x_{j+\frac{1}{2}})$ and $U^-_{j+\frac{1}{2}}:=p_j(t,x_{j+\frac{1}{2}})$, where the $p_j(t,x)$ are non-oscillatory linear polynomial reconstructions, which are used to obtain a second order scheme. In the numerical experiments below, we have used a linear piecewise minmod reconstruction to obtain a second order scheme. Namely, $p_j(t,x)=\bar{U}_j+s_m(t)(x-x_j)$, where

$$s_m(t):=minmod\left(\theta\frac{\bar{U}_{j+1}-\bar{U}_j}{\Delta x},\frac{\bar{U}_{j+1}-\bar{U}_{j-1}}{2\Delta x},\theta\frac{\bar{U}_j-\bar{U}_{j-1}}{\Delta x}\right), \tag{2.14}$$

with

$$minmod(x_1,x_2,\cdots):=\begin{cases}\min(x_i), & \text{if } x_i>0\ \ \forall i,\\ \max(x_i), & \text{if } x_i<0\ \ \forall i,\\ 0, & \text{otherwise,}\end{cases} \tag{2.15}$$

and $\theta\in[1,2]$.

Meanwhile, the one-sided local speeds of propagation $a^\pm_{j+\frac{1}{2}}$ are given by

$$a^+_{j+\frac{1}{2}}:=\max\left(\lambda_{\max}\Big(\frac{\partial F}{\partial U}(U^+_{j+\frac{1}{2}})\Big),\lambda_{\max}\Big(\frac{\partial F}{\partial U}(U^-_{j+\frac{1}{2}})\Big),0\right), \tag{2.16a}$$

$$a^-_{j+\frac{1}{2}}:=\min\left(\lambda_{\min}\Big(\frac{\partial F}{\partial U}(U^+_{j+\frac{1}{2}})\Big),\lambda_{\min}\Big(\frac{\partial F}{\partial U}(U^-_{j+\frac{1}{2}})\Big),0\right). \tag{2.16b}$$

where $\lambda_{\max}(\frac{\partial F}{\partial U}(\tilde{U}))$ and $\lambda_{\min}(\frac{\partial F}{\partial U}(\tilde{U}))$ are the largest and smallest eigenvalues of the differential $\frac{\partial F}{\partial U}$ at the point $U=\tilde{U}$.

Consequently, the approximation of (2.11) now becomes:

$$\frac{d}{dt}\bar{U}_j(t)+\frac{F_{j+\frac{1}{2}}(t)-F_{j-\frac{1}{2}}(t)}{\Delta x}=S_j(t), \tag{2.17}$$

where the approximations of the spatial integrals of the source terms over the j-cell I_j is obtained by using the midpoint rule for the spatial integrals, that is,

$$S_j(t):=S(U(t,x_j),t,x_j). \tag{2.18}$$

We remark that (2.17) is valid for the j-cells I_j, $2\le j\le M$ only. For the boundary cells $j=1$ or $j=M+1$, there are no information from the other sides. Thus, we have to adopt other methods to deal with these cells. We also note that when computing the fluxes at the interface $x=x_{j-\frac{1}{2}}$ or $x=x_{j+\frac{1}{2}}$ for the cells $j=2$ and M, the minmod function can not be applied anymore. In these cases, one-sided difference approximations are applied.

We observe that (2.17) supplemented with the boundary equations $j{=}1,M{+}1$, forms a system of first order ordinary differential equations. Thus, in the numerical simulations, we use a second order Runge-Kutta method (RK2). Let $T>0$ be fixed as above, and set $\Delta t=\frac{T}{N}$, where N is the number of time steps. For $n=0,\cdots,N$, we define U_j^n as the approximate value of U at time $t_n=n\Delta t$, and at the position $x=x_j$. The choice of U_j^0 is taken from the initial data by setting $U_j^0=(u(x_j,0)h(x_j,0),h(x_j,0),v(x_j,0),h_1(x_j,0))^t$ where

$$\begin{aligned}
u(x_j,0)&=\frac{u_1(x_j,0)h_1(x_j,0)+u_2(x_j,0)h_2(x_j,0)}{h(x_j,0)},\\
h(x_j,0)&=h_1(x_j,0)+h_2(x_j,0),\\
v(x_j,0)&=u_1(x_j,0)-u_2(x_j,0).
\end{aligned}$$

The numerical procedure is as follows:

$$\left\{\begin{aligned}
\frac{U_j^*-U_j^n}{\Delta t}&=-\frac{F^n_{j+\frac{1}{2}}-F^n_{j-\frac{1}{2}}}{\Delta x}+S_j^n,\\
\frac{U_j^{**}-U_j^*}{\Delta t}&=-\frac{F^*_{j+\frac{1}{2}}-F^*_{j-\frac{1}{2}}}{\Delta x}+S_j^*,\\
U_j^{n+1}&=\frac{U_j^n+U_j^{**}}{2},
\end{aligned}\right. \tag{2.19}$$

where

$$F^n_{j+\frac{1}{2}}:=F_{j+\frac{1}{2}}(t_n),\qquad S_j^n:=S_j(t_n), \tag{2.20}$$

and $F^*_{j+\frac{1}{2}}$ (resp. $F^{**}_{j+\frac{1}{2}}$) is the value of $F_{j+\frac{1}{2}}(t)$ evaluated at $U_j{=}U_j^*$ (resp. U_j^{**}); S_j^* (resp. S_j^{**}) is the value of $S_j(t)$ evaluated at $U_j=U_j^*$ (resp. U_j^{**}).

Now we describe how to update the boundary values for the barotropic flow. For barotropically subcritical flows, one boundary condition is prescribed at $x=0$ and one boundary condition is prescribed at $x=L$. As we see, these boundary conditions can not give enough information to recover the variables u and h. Fortunately, by inspection of (2.3), we find that the variables α_1 and β_1 satisfy

$$\begin{cases} \dfrac{\partial \alpha_1}{\partial t}+\Big(\dfrac{\alpha_1+3\beta_1}{2}\Big)\dfrac{\partial \alpha_1}{\partial x}=-g\dfrac{\partial B}{\partial x}, \\ \dfrac{\partial \beta_1}{\partial t}+\Big(\dfrac{3\alpha_1+\beta_1}{2}\Big)\dfrac{\partial \beta_1}{\partial x}=-g\dfrac{\partial B}{\partial x}. \end{cases} \tag{2.21}$$

Thus, we can recover the variables u and h by solving (2.21) numerically at the boundary.

For convenience in notation, we denote by $\alpha_{i,j}^n$ (resp. $\beta_{i,j}^n$) the approximate values of α_i (resp. β_i) at $x=x_j$ and $t=t_n$, for $i=1,2$, $1\le j\le M+1$ and $0\le n\le N$.

In the case of the boundary condition (2.5), since the value $\alpha_{1,1}^{n+1}=\alpha_1(0,(n+1)\Delta t)$ is known, we need to approximate $\beta_{1,1}^{n+1}$. For that purpose, we solve the second equation (2.20) numerically. That is, we have

$$\frac{\beta_{1,1}^{n+1}-\beta_{1,1}^n}{\Delta t}+\Big(\frac{3\alpha_{1,1}^n+\beta_{1,1}^n}{2}\Big)\frac{\beta_{1,2}^{n+1}-\beta_{1,1}^{n+1}}{\Delta x}=-gB_{x,1}, \tag{2.22}$$

where $B_{x,1}$ is the first derivative approximation of $B(x)$ evaluated at $x=x_1$.

To update the boundary value $\beta_{1,1}^{n+1}$, we need the value $\beta_{1,2}^{n+1}$ which has been updated by solving the ordinary differential equation (2.18). Combining with the proposed boundary conditions (the first equation of (2.5)), the approximate values (u^{n+1}, h^{n+1}) at $x=0$ can be totally determined.

For $x=L$, we have similarly

$$\frac{\alpha_{1,M+1}^{n+1}-\alpha_{1,M+1}^n}{\Delta t}+\Big(\frac{\alpha_{1,M+1}^n+3\beta_{1,M+1}^n}{2}\Big)\frac{\alpha_{1,M+1}^{n+1}-\alpha_{1,M}^{n+1}}{\Delta x}=-gB_{x,M+1}. \tag{2.23}$$

Since the value $\alpha_{1,M}^{n+1}$ has been updated by solving the ordinary differential equation (2.18), the boundary value $\alpha_{1,M+1}^{n+1}$ can be determined by (2.23). Combining with the proposed boundary conditions (the second equation of (2.5)), the approximate values (u^{n+1}, h^{n+1}) at $x=L$ can be totally determined. Then, the approximate values for barotropically subcritical flows have been updated.

As for barotropically supercritical flows, two boundary conditions (2.4) are prescribed at $x=0$ and no boundary condition is prescribed at $x=L$. Therefore, the information at $x=0$ is known. For $x=L$, we can compute the variables u and h by solving (2.21) numerically. That is, we have

$$\frac{\beta_{1,M+1}^{n+1}-\beta_{1,M+1}^n}{\Delta t}+\Big(\frac{3\alpha_{1,M+1}^n+\beta_{1,M+1}^n}{2}\Big)\frac{\beta_{M+1,2}^{n+1}-\beta_{M,1}^{n+1}}{\Delta x}=-gB_{x,M+1}, \tag{2.24}$$

along with (2.23).

Since the values $\alpha_{1,M}^{n+1}$ and $\beta_{1,M}^{n+1}$ have been updated by solving the ordinary differential equation (2.18), the approximate values $(u^{n+1},\ h^{n+1})$ can be determined and then the approximate values for the barotropically supercritical flow are fully computed.

To completely determine the approximate values U_j for all j, we need to update similarly the boundary values v^{n+1} and h_1^{n+1} at $x=0$ and $x=L$.

Now, we describe how to update the boundary values for baroclinic flows. For baroclinically subcritical flows, one boundary condition is prescribed at $x=0$ and one boundary condition is prescribed at $x=L$. This case is similar to the case of barotropically subcritical flows. Therefore, we need more information to recover the variables v and h_1. Following (2.4), we find that the variables α_2 and β_2 satisfy

$$\begin{cases} \dfrac{\partial \alpha_2}{\partial t}+\left(u+\dfrac{v(h-2h_1)}{h}+\dfrac{1}{h}\sqrt{h_1(h-h_1)(g'h-v^2)}\right)\dfrac{\partial \alpha_2}{\partial x}=0, \\ \dfrac{\partial \beta_2}{\partial t}+\left(u+\dfrac{v(h-2h_1)}{h}-\dfrac{1}{h}\sqrt{h_1(h-h_1)(g'h-v^2)}\right)\dfrac{\partial \beta_2}{\partial x}=0. \end{cases} \tag{2.25}$$

Thus, we can recover the variables v and h_1 by solving (2.25) numerically at the boundary. Namely, we have at $x=0$

$$\begin{aligned} &\frac{\beta_{2,1}^{n+1}-\beta_{2,1}^{n}}{\Delta t}+\left(u_1^n+\frac{v_1^n(h_1^n-2h_{1,1}^n)}{h_1^n}\right. \\ &\qquad\left.-\frac{1}{h_1^n}\sqrt{h_{1,1}^n(h_1^n-h_{1,1}^n)(g'h_1^n-(v_1^n)^2)}\right)\frac{\beta_{2,2}^{n+1}-\beta_{2,1}^{n+1}}{\Delta x}=0, \end{aligned} \tag{2.26}$$

and at $x=L$

$$\begin{aligned} &\frac{\alpha_{2,M+1}^{n+1}-\alpha_{2,M+1}^{n}}{\Delta t}+\left(u_{M+1}^n+\frac{v_{M+1}^n(h_{M+1}^n-2h_{1,M+1}^n)}{h_{M+1}^n}\right. \\ &\quad\left.+\frac{1}{h_{M+1}^n}\sqrt{h_{1,M+1}^n(h_{M+1}^n-h_{1,M+1}^n)(g'h_{M+1}^n-(v_{M+1}^n)^2)}\right)\frac{\alpha_{2,M+1}^{n+1}-\alpha_{2,M}^{n+1}}{\Delta x}=0. \end{aligned} \tag{2.27}$$

Since the values $\beta_{2,2}^{n+1}$ and $\alpha_{2,M}^{n+1}$ have been updated by solving the ordinary differential equation (2.18), the values $\beta_{2,1}^{n+1}$ and $\alpha_{2,M+1}^{n+1}$ can be determined by (2.26) and (2.27). Then, the approximate values $(v^{n+1},\ h_1^{n+1})$ can be fully computed.

As for baroclinically supercritical flows, this case is similar to the case of the barotropically supercritical flows. Therefore, we need to numerically solve (2.25) at $x=L$. That is, we have

$$\begin{aligned} &\frac{\beta_{2,M+1}^{n+1}-\beta_{2,M+1}^{n}}{\Delta t}+\left(u_{M+1}^n+\frac{v_{M+1}^n(h_{M+1}^n-2h_{1,M+1}^n)}{h_{M+1}^n}\right. \\ &\quad\left.-\frac{1}{h_{M+1}^n}\sqrt{h_{1,M+1}^n(h_{M+1}^n-h_{1,M+1}^n)(g'h_{M+1}^n-(v_{M+1}^n)^2)}\right)\frac{\beta_{2,M+1}^{n+1}-\beta_{2,M}^{n+1}}{\Delta x}=0, \end{aligned} \tag{2.28}$$

along with (2.27).

Similarly, the values $\alpha_{2,M}^{n+1}$ and $\beta_{2,M}^{n+1}$ have been updated by solving the ordinary differential equation (2.18) and then the approximate boundary values (v^{n+1}, h_1^{n+1}) are determined. Finally, the approximate values (v^{n+1}, h_1^{n+1}) can be fully computed.

We refer the reader to the cited articles for more detailed information.

2.2 Numerical simulations

Now, we present several examples for which we tested the proposed boundary conditions. In all cases, the gravitational constant is taken as $g{=}9.812m/s^2$, the reduced gravity $g'=1m/s^2$, and the length of the physical domain is taken as $L=10^3km$. The Courant-Friedrichs-Lewy (CFL) number is chosen satisfying the hyperbolic CFL condition.

Example One: small perturbation of a steady state flow

The first example is modified from an example in [2]. The bottom topography consists of one hump,

$$B(x)=\begin{cases} \dfrac{\delta}{2}+\dfrac{\delta}{2}\cos\Big(\dfrac{\pi(x-\frac{L}{2})}{\kappa}\Big), & \text{if } \Big|x-\dfrac{L}{2}\Big|\le\kappa,\\ 0, & \text{otherwise,}\end{cases} \tag{2.29}$$

where δ controls the height of the hump, and κ measures the width of the hump. In this example, we take the height of the hump $\delta=5\times10^3$ m and the width of the hump $\kappa=L/10$.

The initial data is the stationary solution with a small perturbation,

$$\begin{aligned} &u(x,0)=u_0, \qquad v(x,0)=v_0,\\ &h_1(x,0)=h_{1,0}-B(x), \qquad h(x,0)=\begin{cases} h_0-B(x)+\epsilon h_0, & \text{if } \kappa\le x\le 2\kappa,\\ h_0-B(x), & \text{otherwise.}\end{cases}\end{aligned}$$

Here $u_0=0$ m/s, $v_0=0$ m/s, $h_{1,0}=7000$ m, $h_0=10^4$ m and the nonzero constant parameter ϵ which controls the amplitude of the perturbation is taken as $\epsilon=0.2$ or -0.2. This example is the case of a barotropically and baroclinically subcritical flow. Thus, boundary conditions (2.5) and (2.7) are applied.

Figs. 2 and 5 show the computed free surfaces $h+B(x)$ and $h_1+B(x)$ at different times. The computation time T is taken to be 72000 seconds. In all simulations the number of grid points is taken as $M=400$ and the number of time steps is $N=5\times10^5$. The results are shown for different parameters $\epsilon=-0.2,0.2$.

Figs. 3 and 6 show the time evolution of the kinetic energy for the lower layer and the upper layer. Figs. 4 and 7 show the time evolution of the mass flux for the lower and upper layers at the boundary point $x=0$ and L.

As shown in Figs. 2 and 5, the initial small perturbation produces two barotropic (baroclinic) waves propagating at the characteristic speeds $\pm\sqrt{gh}(\pm\sqrt{g'h_1h_2/h})$. The

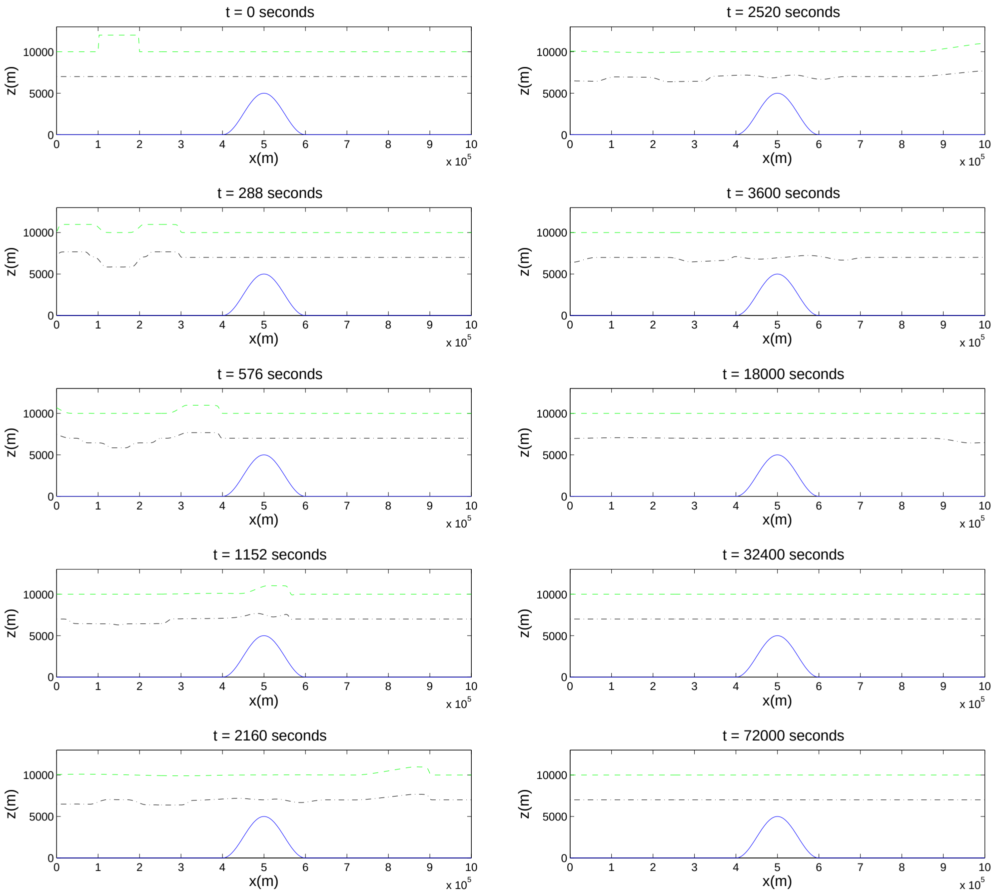

Figure 2: The height of the free surfaces $h+B(x)$ and $h_1+B(x)$ at different times where $\epsilon=0.2$. The dashed line represents the height of the free surface $h+B(x)$ (top of the higher layer of fluid) and the dashdot line represents the height of the free surface $h_1+B(x)$ (top of the lower layer of fluid).

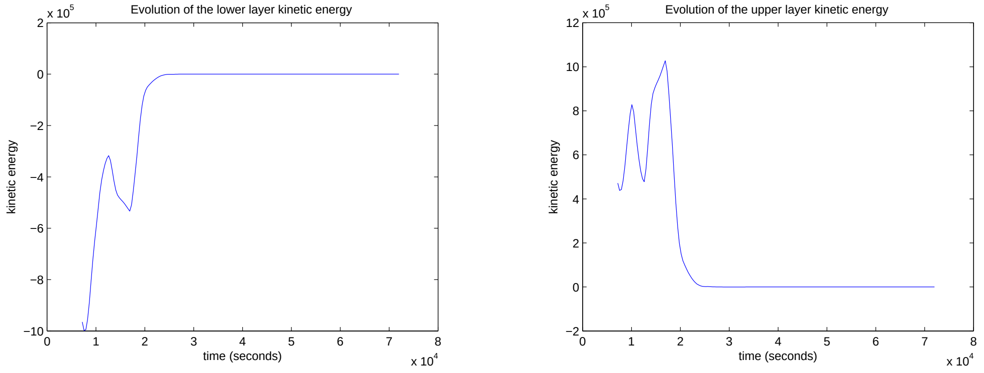

Figure 3: The time evolution of the kinetic energy for the lower layer (on the left) and the upper layer (on the right) where $\epsilon=0.2$.

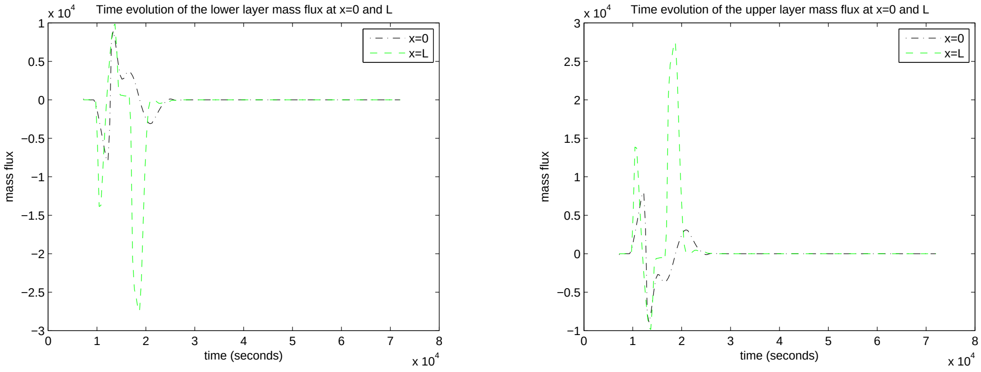

Figure 4: The time evolution of the mass flux for the lower layer energy E_1 (on the left) and the upper layer energy E_2 (on the right) at $x=0$ and L where $\epsilon=0.2$.

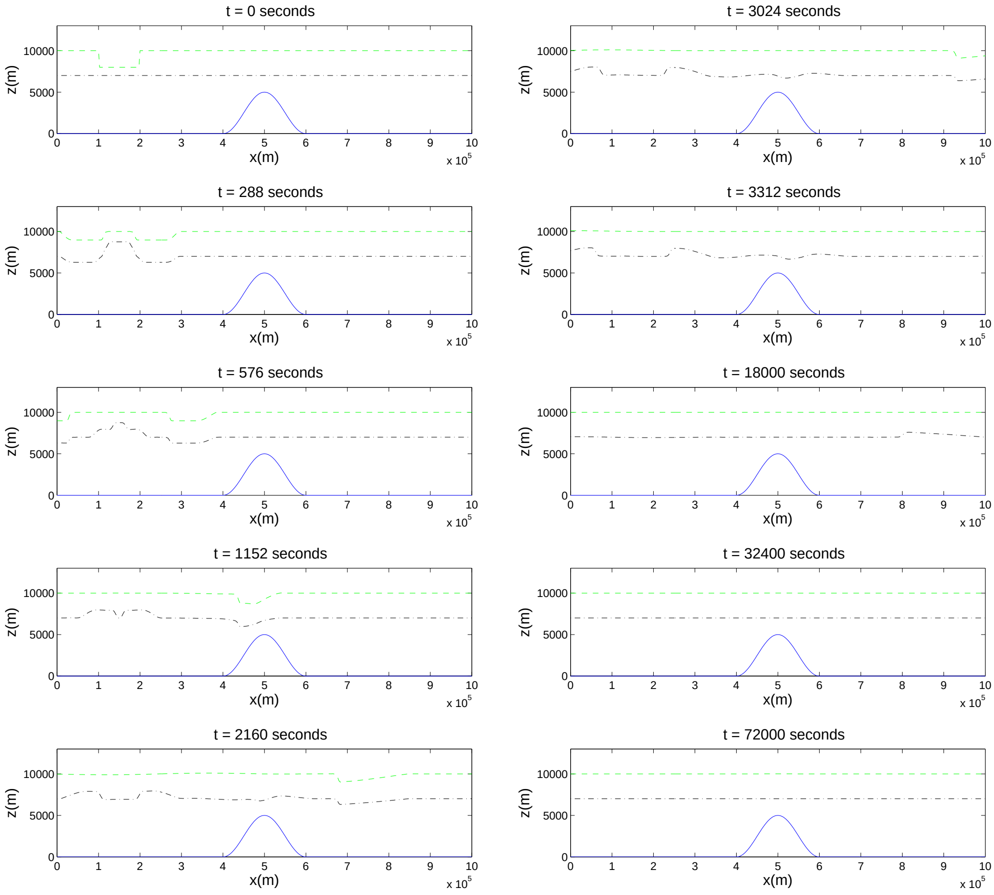

Figure 5: The height of the free surfaces $h+B(x)$ and $h_1+B(x)$ at different times where $\epsilon=-0.2$. The dashed line represents the height of the free surface $h+B(x)$ (top of the higher layer of fluid) and the dashdot line represents the height of the free surface $h_1+B(x)$ (top of the lower layer of fluid).

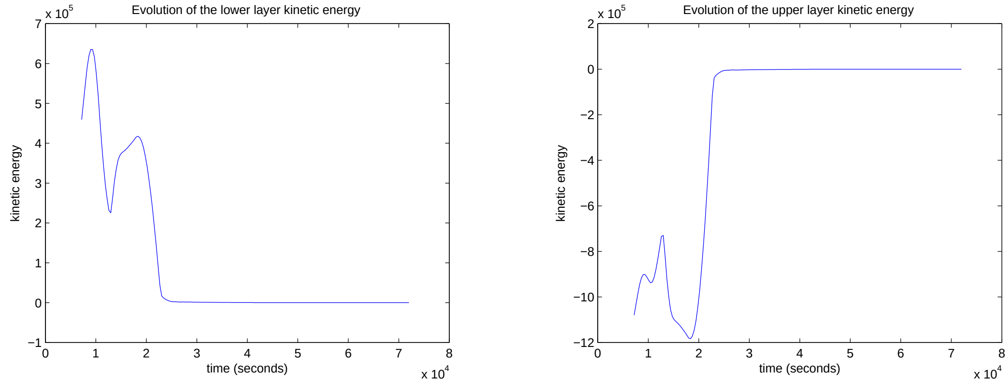

Figure 6: The time evolution of the kinetic energy for the lower layer (on the left) and the upper layer (on the right) where $\epsilon = -0.2$.

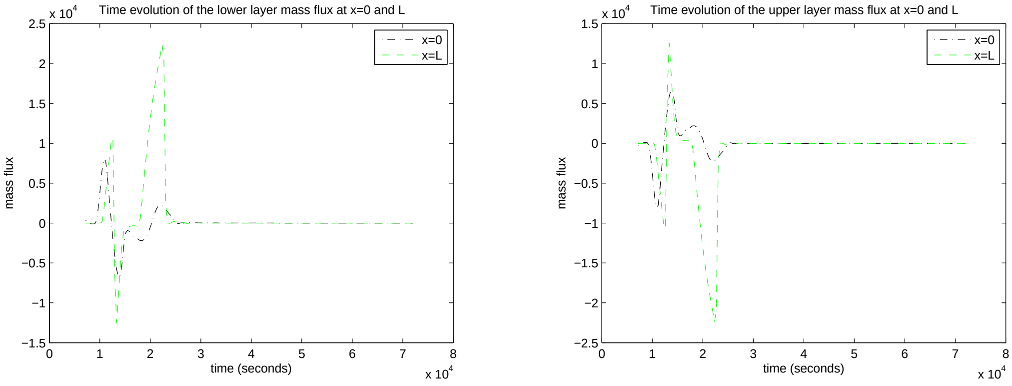

Figure 7: The time evolution of the mass flux for the lower layer energy E_1 (on the left) and the upper layer energy E_2 (on the right) at $x=0$ and L where $\epsilon = -0.2$.

barotropic waves flow out of the domain freely. After approximately 3600 seconds, the barotropic waves become stationary and then the remaining waves are baroclinic. Since the speed of the baroclinic waves is smaller, the internal disturbance takes a longer time to get out of the domain freely. Furthermore, as shown in Figs. 3, 4, 6 and 7, the mass flux and energy in each layer are close to the steady state after all the perturbation waves get out of the domain, indicating that the proposed boundary conditions are suitable.

Example Two: small global perturbation of the quasi-steady flow

In this example, we consider the quasi-steady flow in which the momentum uh is a nonzero constant in the barotropic mode with a small global perturbation and choose different values of u_0 to perform the numerical simulations of the baroclinically subcritical and supercritical flows, respectively. We begin with the following initial data:

$$\begin{cases} u(x,0)=\dfrac{u_0}{1+\varepsilon}\left(1+\varepsilon\cos\left(\dfrac{2\pi mx}{L}\right)\right), \\ v(x,0)=v_0, \\ h_1(x,0)=h_{1,0}-B(x), \\ h(x,0)=\dfrac{h_0}{1+\varepsilon}\left(1+\varepsilon\cos\left(\dfrac{2\pi mx}{L}\right)\right), \end{cases} \tag{2.30}$$

where the parameter ε controls the magnitude of the perturbation and is taken as $\varepsilon=0.1$, and $m=20$ is the frequency of the perturbed wave. Here we take

$$u_0=10,\quad \text{or}\quad 60\text{m/s},\ v_0=0\text{m/s},\ h_{1,0}=7000\text{m}\quad \text{and}\quad h_0=10^4\text{m},$$

and the bottom $B(x)$ is given by Eq. (2.29) with $\delta=4\times10^3$ m and $\kappa=L/10$.

When u_0 is chosen as 10 (60) m/s, the flow is barotropically and baroclinically subcritical (barotropically subcritical and baroclinically supercritical), respectively. The boundary conditions (2.5) and (2.7) (respectively (2.5) and (2.8)) are applied. The initial condition (2.30) and the given corresponding boundary conditions satisfy certain compatibility conditions.

Fig. 8 shows the computed free surfaces $h+B(x)$ and $h_1+B(x)$ at different times for the case of the barotropically subcritical-baroclinically subcritical flow. The computation time T is taken to be 72000 seconds. Fig. 11 shows the computed free surfaces $h+B(x)$ and $h_1+B(x)$ at different times for the case of the barotropically subcritical-baroclinically supercritical flow. The computation time T is taken to be 72000 seconds. As Example One, the time evolution of the kinetic energy for the lower layer and the upper layer is plotted in Figs. 9 and 12 and the time evolution of the mass flux for the lower and upper layers at the boundary point $x=0$ and L is presented in Figs. 10 and 13. In all simulations the number of grid points is taken as $M=400$ and the number of time steps is $N=5\times10^5$.

In Fig. 8, we observe that barotropic and baroclinic waves generated by small global perturbations flow out of the domain freely. This result is similar to Example One.

In Fig. 11, the evolution of the flow is generated by a small global perturbation. The barotropic waves have a quick response and then they move out of the domain freely. Due to the presence of the hump, the baroclinic waves form a propagating shock on the downwind side and take a smaller speed to travel. Moreover, both barotropic and baroclinic waves move out of the domain freely.

All calculations shown in Figs. 9, 10, 12 and 13 confirm the suitability of the proposed boundary conditions.

Example Three: barotropically supercritical flow

This problem is modified from [34] in which the authors studied the single-layer shallow water equations. We start with the following initial data:

$$u(x,0)=u_0,\quad v(x,0)=v_0,\quad h_1(x,0)=h_{1,0}-B(x),\quad h(x,0)=h_0-B(x), \tag{2.31}$$

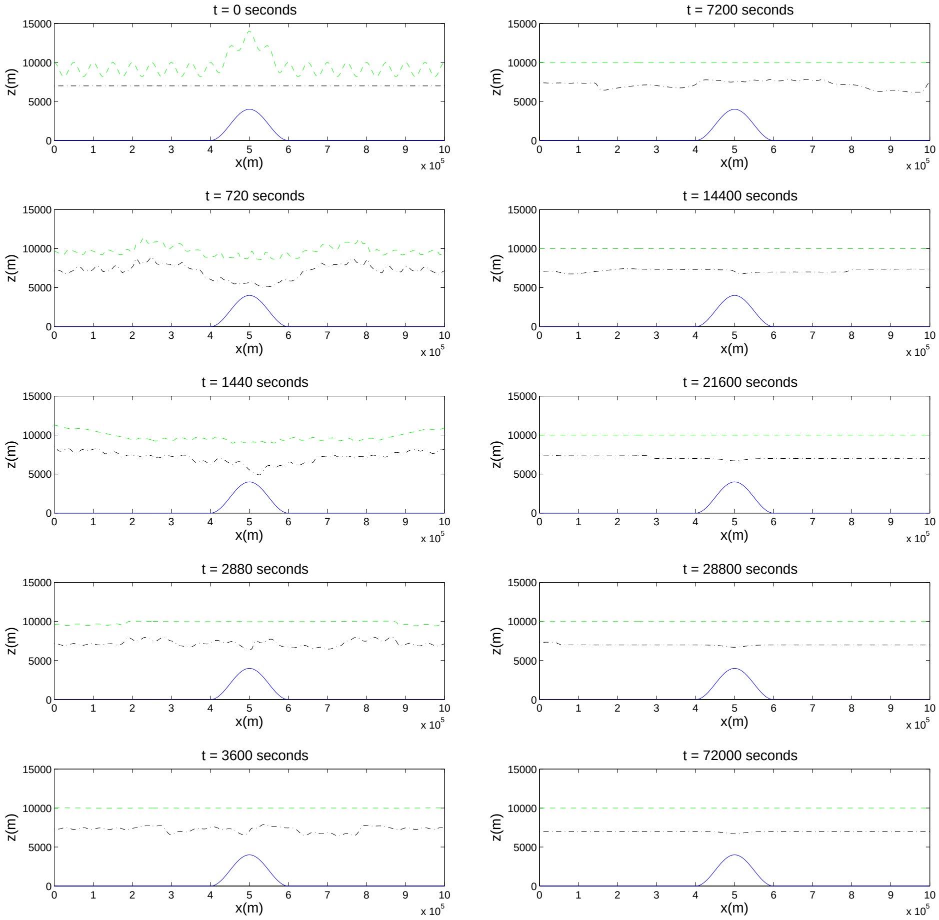

Figure 8: The height of the free surfaces $h+B(x)$ and $h_1+B(x)$ at different times in the case of barotropically and baroclinically subcritical flows. The dashed line represents the height of the free surface $h+B(x)$ (top of the higher layer of fluid) and the dashdot line represents the height of the free surface $h_1+B(x)$ (top of the lower layer of fluid).

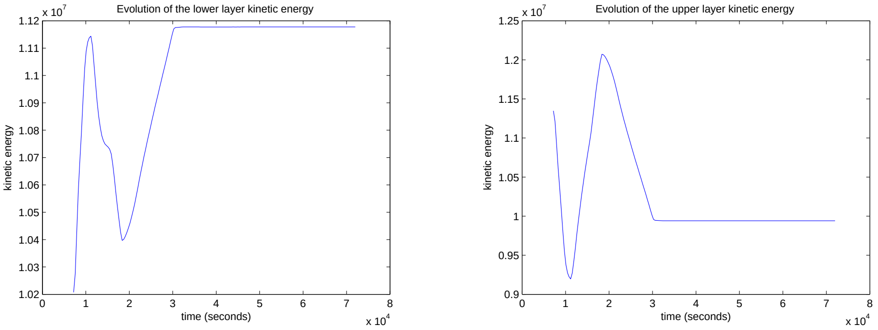

Figure 9: The time evolution of the kinetic energy for the lower layer (on the left) and the upper layer (on the right) in the case of barotropically and baroclinically subcritical flows.

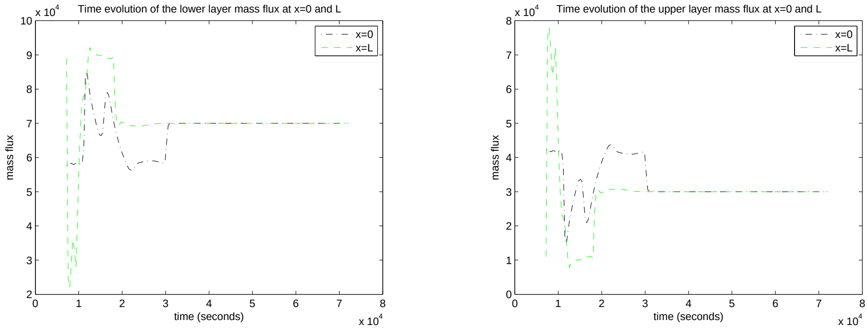

Figure 10: The time evolution of the mass flux for the lower layer energy E_1 (on the left) and the upper layer energy E_2 (on the right) at $x=0$ and L in the case of barotropically and baroclinically subcritical flows.

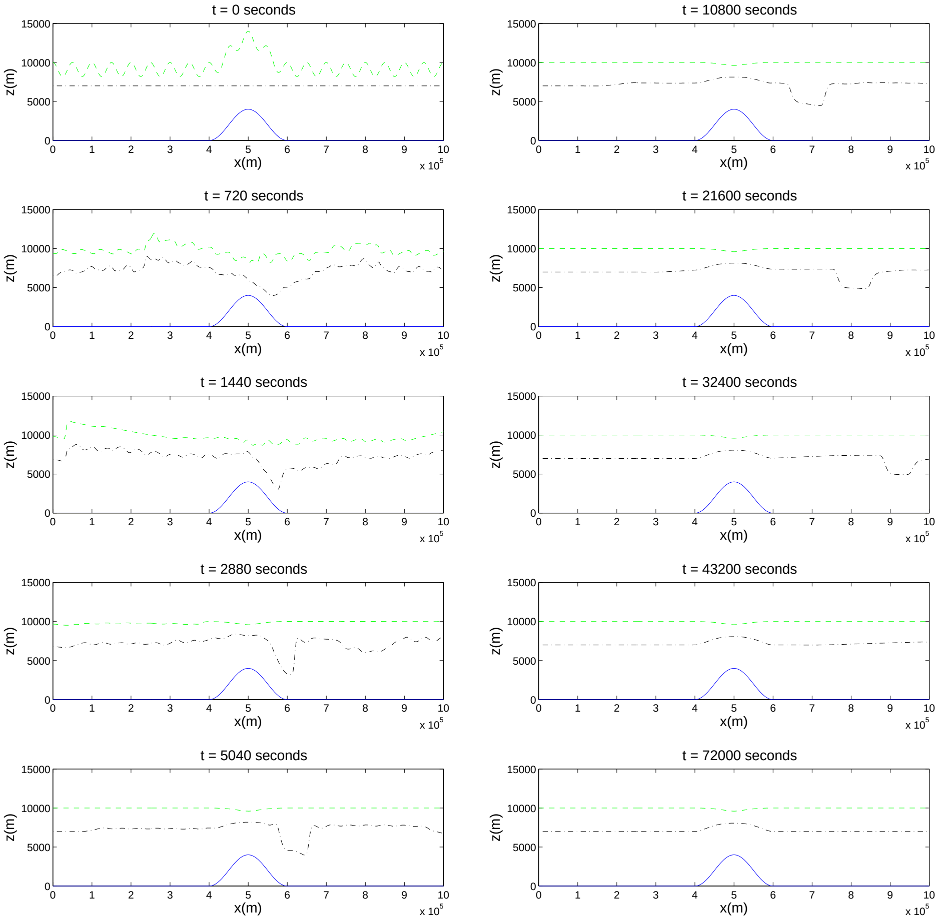

Figure 11: The height of the free surfaces $h+B(x)$ and $h_1+B(x)$ at different times in the case of barotropically subcritical and baroclinically supercritical flows. The dashed line represents the height of the free surface $h+B(x)$ (top of the higher layer of fluid) and the dashdot line represents the height of the free surface $h_1+B(x)$ (top of the lower layer of fluid).

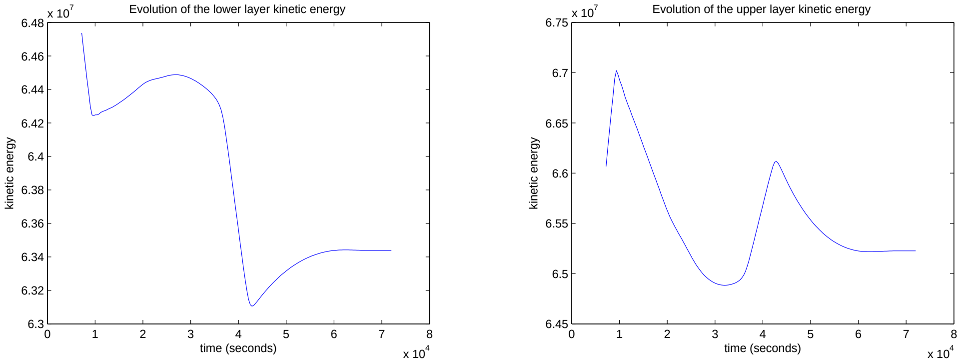

Figure 12: The time evolution of the kinetic energy for the lower layer (on the left) and the upper layer (on the right) in the case of barotropically subcritical and baroclinically supercritical flows.

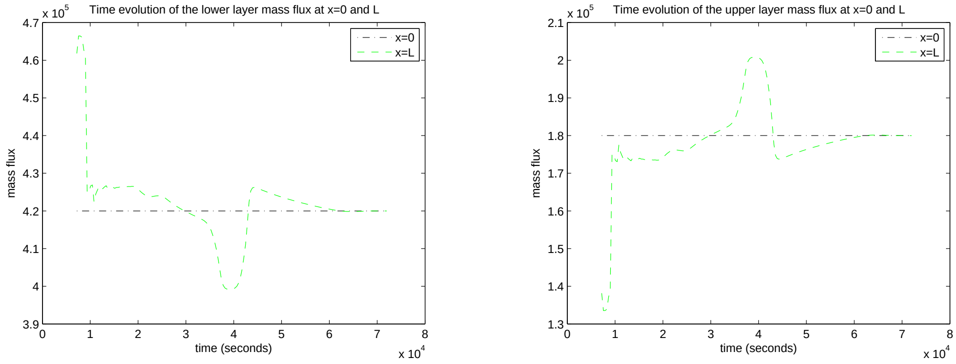

Figure 13: The time evolution of the mass flux for the lower layer energy E_1 (on the left) and the upper layer energy E_2 (on the right) at $x=0$ and L in the case of barotropically subcritical and baroclinically supercritical flows.

where $u_0=450$ m/s, $v_0=0$ m/s, $h_{1,0}=3\times10^3$ m, $h_0=5\times10^3$ m, and $B(x)$ is given by (2.29) with $\delta=10^3$ m, and $\kappa=L/10$. Note that the chosen value $u_0=450$ m/s is not a realistic speed for flows on the Earth. We chose to keep the geometry unchanged by taking this large unrealistic speed $u_0=450m/s$. As explained in [34], this flow produces the same nondimensional flow as a realistic one. In this example, the boundary conditions (2.6) and (2.8) are applied since a barotropically supercritical flow is also baroclinically supercritical.

Fig. 14 shows the computed free surfaces $h+B(x)$ and $h_1+B(x)$ at different times. The computation time T is taken to be 4800 seconds. Fig. 15 shows the time evolution of the kinetic energy for the lower layer and the upper layer. Fig. 16 shows the time evolution of the mass flux for the lower and upper layers at the boundary point $x=0$ and L. In all the simulations, the number of grid points is taken as $M=400$ and the number of time steps is $N=5\times10^5$.

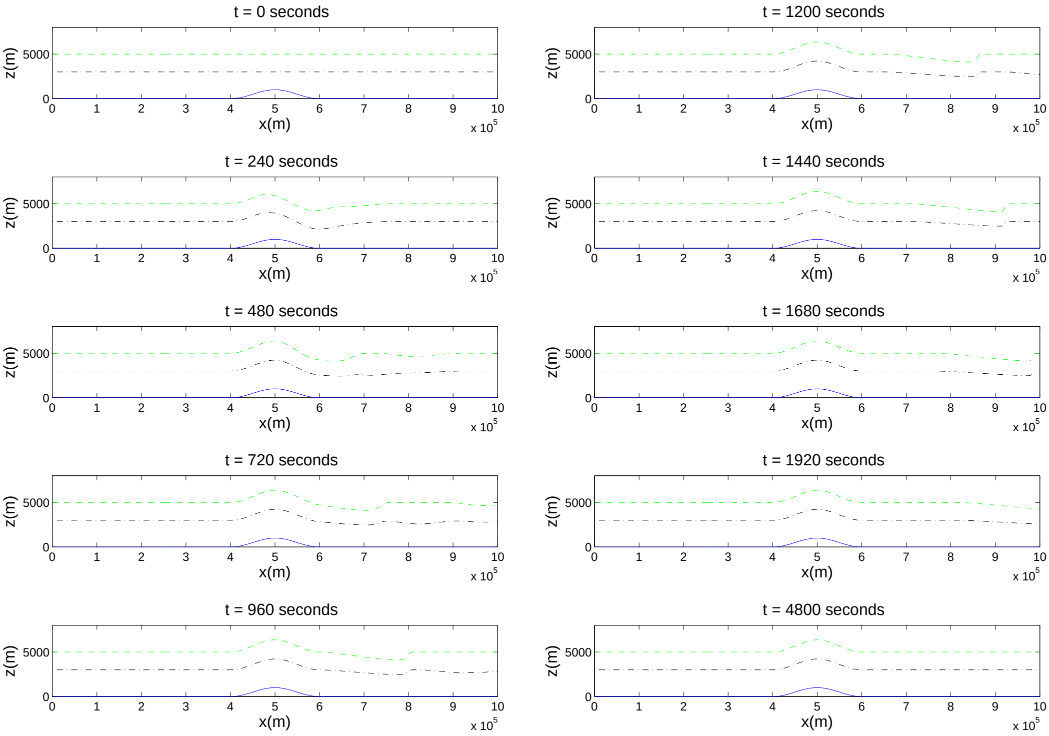

Figure 14: The height of the free surfaces $h+B(x)$ and $h_1+B(x)$ at different times in the case of barotropically supercritical flows. The dashed line represents the height of the free surface $h+B(x)$ (top of the higher layer of fluid) and the dashdot line represents the height of the free surface $h_1+B(x)$ (top of the lower layer of fluid).

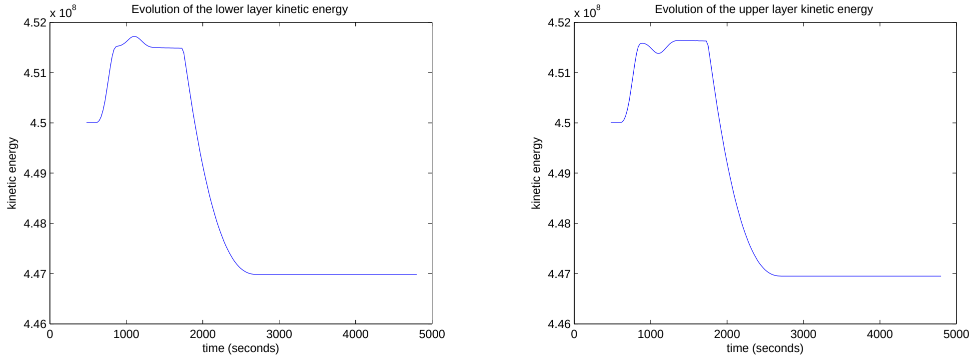

Figure 15: The time evolution of the kinetic energy for the lower layer (on the left) and the upper layer (on the right) in the case of barotropically supercritical flows.

In Fig. 14, we observe that the free surfaces $h+B(x)$ and $h_1+B(x)$ of the steady state produce a large elevation of the surface above the hump. Also, since the wave speed dominates the gravity speed in this case, barotropic and baroclinic waves reach the steady

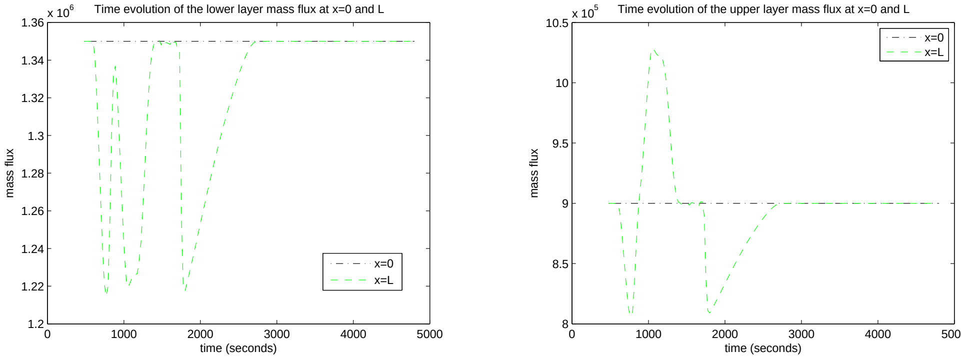

Figure 16: The time evolution of the mass flux for the lower layer energy E_1 (on the left) and the upper layer energy E_2 (on the right) at $x=0$ and L in the case of barotropically supercritical flows.

state at almost the same time and move out of the domain freely. Furthermore, as shown in Figs. 15 and 16, the mass flux and energy in each layer are close to the steady state after all the perturbation waves get out of the domain, indicating that the proposed boundary conditions are suitable.

Example Four: testing in a nested environment

In this example, we intend to test our proposed boundary conditions in a nested environment. Two different simulations are performed. An initial simulation is performed on the larger domain $D_l=\{0<x<L\}$. Using the data obtained from the initial simulation as boundary conditions on the middle domain $D_m=\{L/3<x<2L/3\}$, we carry out the second simulation on this interior domain. Then we compare these two results over the middle domain.

The testing cases we choose are similar to those in Example One with flat bottoms $(B=0)$. In the simulation on the larger domain D_l, the initial conditions are given as

$$\begin{aligned}&u(x,0)=u_0, \qquad v(x,0)=v_0,\\&h_1(x,0)=h_{1,0}, \qquad h(x,0)=\begin{cases} h_0+\epsilon h_0, & \text{if } L-2\kappa\le x\le L-\kappa,\\ h_0, & \text{otherwise.}\end{cases}\end{aligned}$$

Here $u_0=0$ m/s ,$v_0=0$ m/s ,$h_{1,0}=7000$ m ,$h_0=10^4$ m , the nonzero constant parameter ϵ is taken as $\epsilon=0.2$ or -0.2 and $\kappa=L/10$. In the simulation, the boundary conditions are chosen to satisfy (2.5) and (2.7). In this example, the length of the domain is taken as $L=3\times10^3$ km and the final time is taken as $T=72000$ seconds. In the simulation, the number of grid points is taken as $M=1200$ and the number of time steps is $N=5\times10^5$.

Next, we do simulations on the middle domain D_m of the larger domain D_l. The boundary values are inferred from the previous simulation. More specifically, the chosen

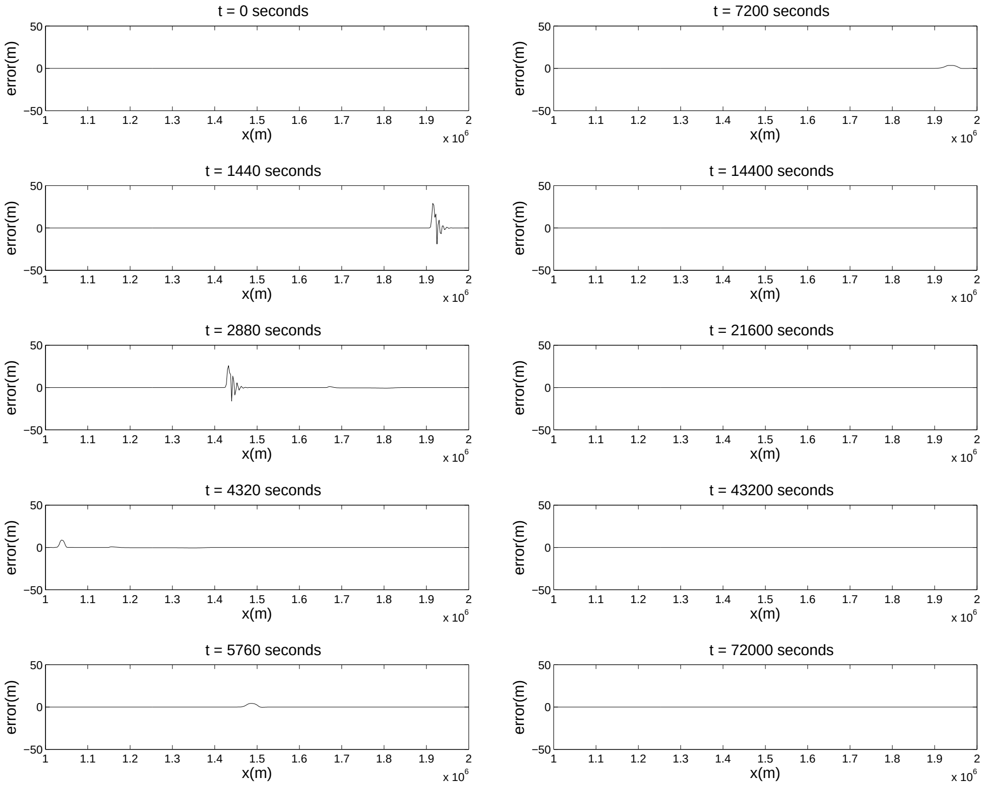
t = 0 seconds

t = 7200 seconds

t = 1440 seconds

t = 14400 seconds

t = 2880 seconds

t = 21600 seconds

t = 4320 seconds

t = 43200 seconds

t = 5760 seconds

t = 72000 seconds

Figure 17: The actual value of the errors over the middle domain at different times for the height h in the case of $\epsilon=0.2$.

boundary conditions are given as follows:

$$\begin{cases} u^m(\frac{L}{3},t)+2\sqrt{gh^m(\frac{L}{3},t)}=u^l(\frac{L}{3},t)+2\sqrt{gh^l(\frac{L}{3},t)},\\ u^m(\frac{2L}{3},t)-2\sqrt{gh^m(\frac{2L}{3},t)}=u^l(\frac{2L}{3},t)-2\sqrt{gh^l(\frac{2L}{3},t)}, \end{cases} \tag{2.32}$$

and

$$\begin{cases} \arcsin\left(\dfrac{v^m(\frac{L}{3},t)}{\sqrt{g'h^m(\frac{L}{3},t)}}\right)-\arcsin\left(\dfrac{h^m(\frac{L}{3},t)-2h_1^m(\frac{L}{3},t)}{h^m(\frac{L}{3},t)}\right)\\ \qquad =-\arcsin\left(\dfrac{h^l(\frac{L}{3},t)-2h_1^l(\frac{L}{3},t)}{h^l(\frac{L}{3},t)}\right),\\ \arcsin\left(\dfrac{v^m(\frac{2L}{3},t)}{\sqrt{g'h^m(\frac{2L}{3},t)}}\right)+\arcsin\left(\dfrac{h^m(\frac{2L}{3},t)-2h_1^m(\frac{2L}{3},t)}{h^m(\frac{2L}{3},t)}\right)\\ \qquad =\arcsin\left(\dfrac{h^l(\frac{2L}{3},t)-2h_1^l(\frac{2L}{3},t)}{h^l(\frac{2L}{3},t)}\right). \end{cases} \tag{2.33}$$

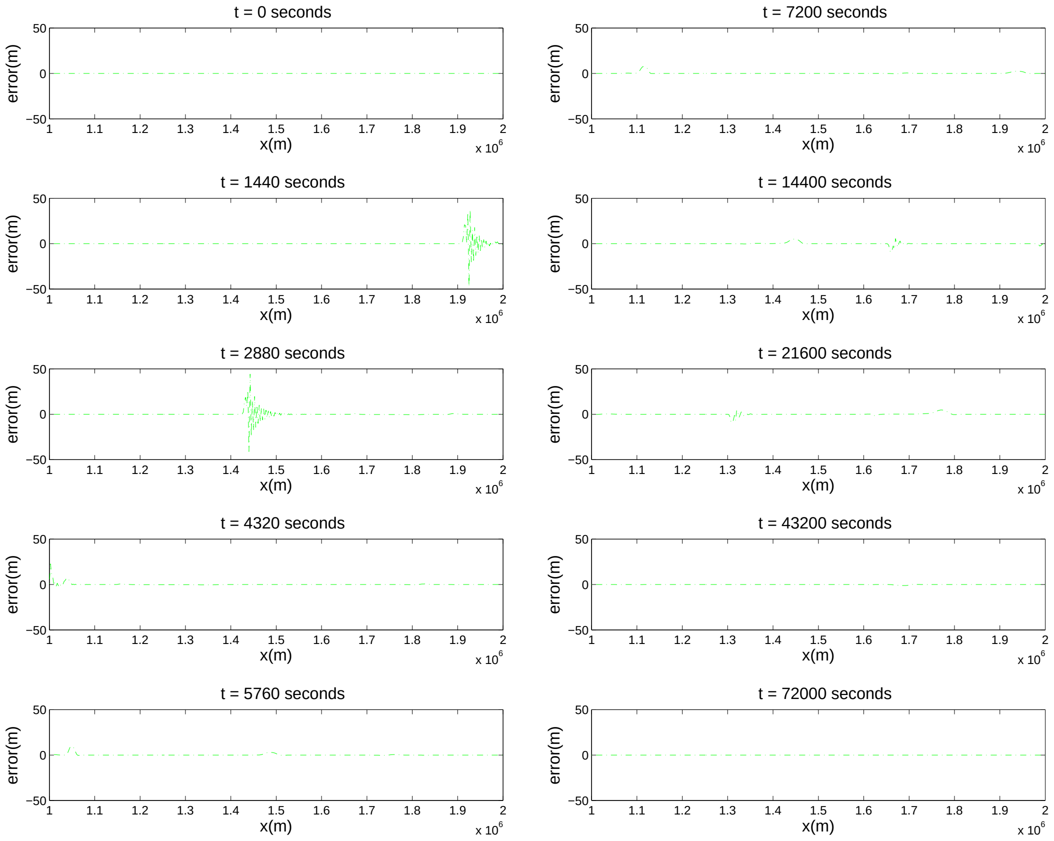

Figure 18: The actual value of the errors over the middle domain at different times for the height h_1 in the case of $\epsilon = 0.2$.

In the above, the superscript l denotes the previous simulation on the larger domain; the superscript m denotes the simulation on the middle domain. In this simulation, we take 400 segments in the x-direction.

We compare these two distinct simulations namely the results of the simulations on the larger domain D_l restricted to the middle domain and the results of the simulations on the middle domain D_m in two different ways:

- Either we compute the relative errors in both L^2 and the L^∞ norms. The relative errors are defined as $\frac{||h^{int}-h^{ext}|_{D_m}|_{L^p}}{|h^{ext}|_{L^p}}$ where the superscript $ext(int)$ denotes the numerical approximation of the variables on the larger domain (on the middle domain), respectively and $p=2,\infty$.
- Or we plot the actual errors.

In Figs. 17-20, we plot the errors of the heights h and h_1 over the middle domain at certain times with different values $\epsilon = 0.2$ or -0.2.

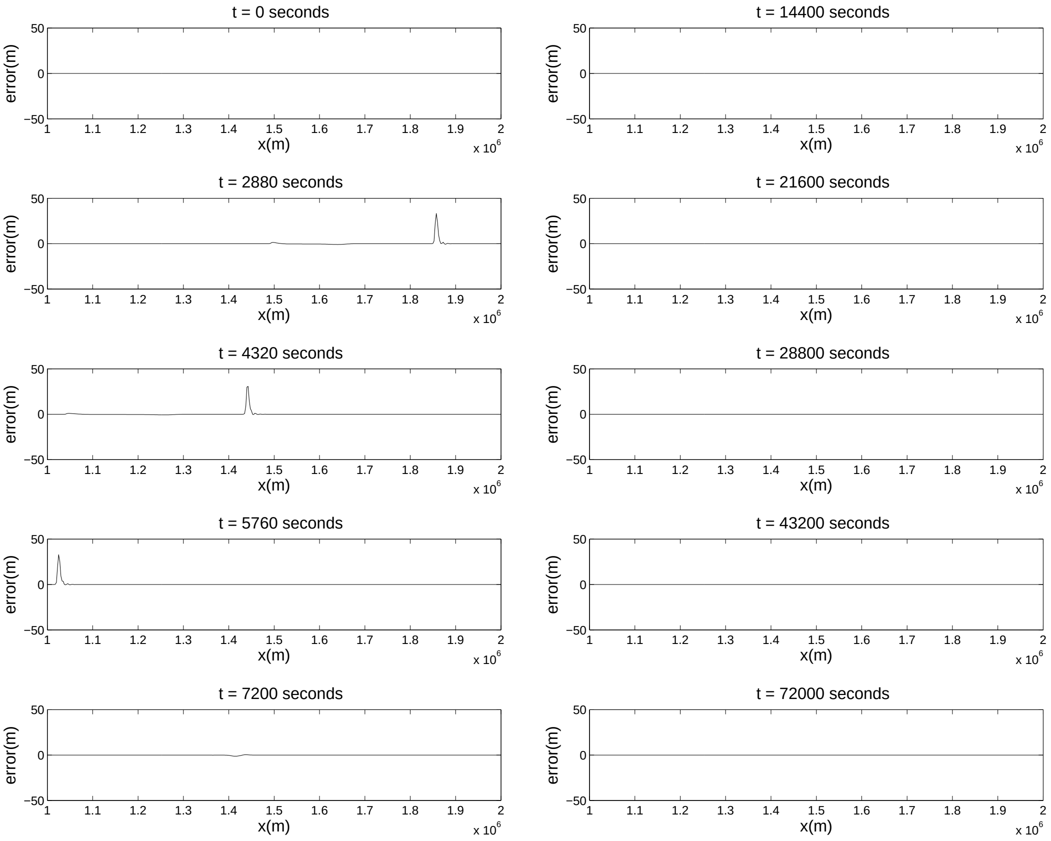

Figure 19: The actual value of the errors over the middle domain at different times for the height h in the case of $\epsilon = -0.2$.

In Figs. 21 and 22, we also plot the evolution of the relative errors for the functions h and h_1, in both the L^2 and the L^∞ norms with different values $\epsilon = 0.2$ or -0.2.

As shown in Figs. 21 and 22, we observe that the relative errors in both the L^2 and the L^∞ norms are of magnitude $\mathcal{O}(10^{-2})$ or smaller, which indicates that the results on the larger domain D_l and the results on the middle domain D_m match very well.

Remark 2.2. A noteworthy computational importance of this work, is that this is, to the best of our knowledge, the only article in which the equations above are numerically treated without any artificial viscosity. In related situation, in [25], the authors added lateral viscosity terms in the momentum equations and performed numerical simulations of both one- and two-layer shallow water models with the proposed nonlinear characteristic open boundary conditions by using finite difference schemes. We do not introduce numerical viscosity and our model is totally inviscid. Moreover, the treatment of the boundary conditions in [25] is to update the values at the boundary by using some values from previous time steps while we determine the values at the boundary by numerically solving the equations satisfied by the introduced characteristic variables.

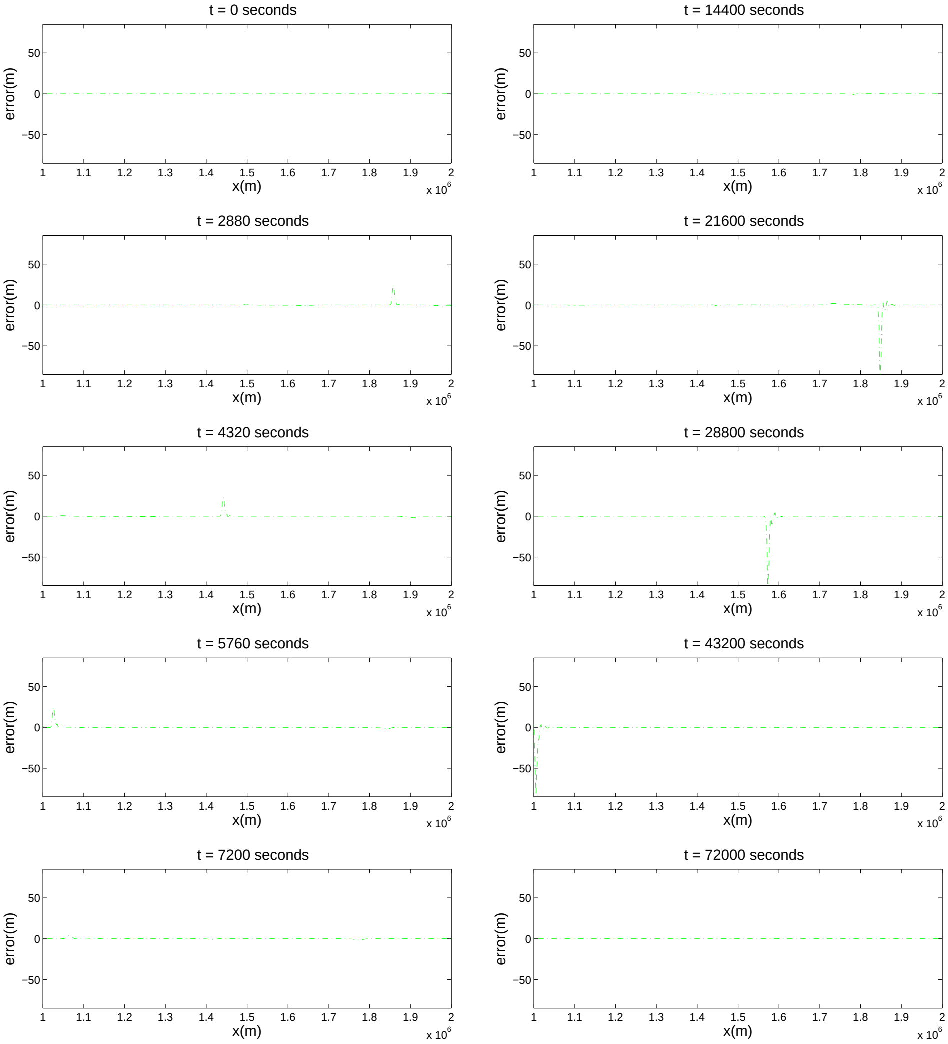

Figure 20: The actual value of the errors over the middle domain at different times for the height h_1 in the case of $\epsilon = -0.2$.

3 The Rossby equatorial soliton: shallow water equations in a rectangle

The equations are slightly different than the usual shallow water equations because we add the Coriolis force. Furthermore, we consider two different boundary conditions: the Dirichlet boundary conditions and the transparent conditions. The test model considered in the geophysical literature is described in details at this address:

`http://marine.rutgers.edu/po/tests/rossby/index.html` ,

and it corresponds to the Dirichlet boundary conditions.

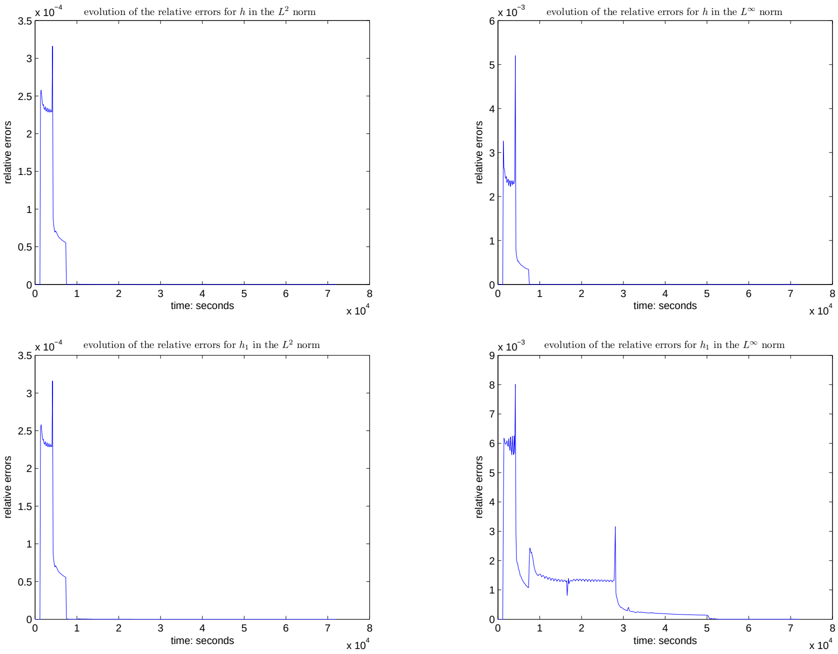

Figure 21: The evolution of the relative errors for the free surfaces h (on the top) and h_1 (on the bottom) in the case of $\epsilon=0.2$ (L^2 and L^∞ norms).

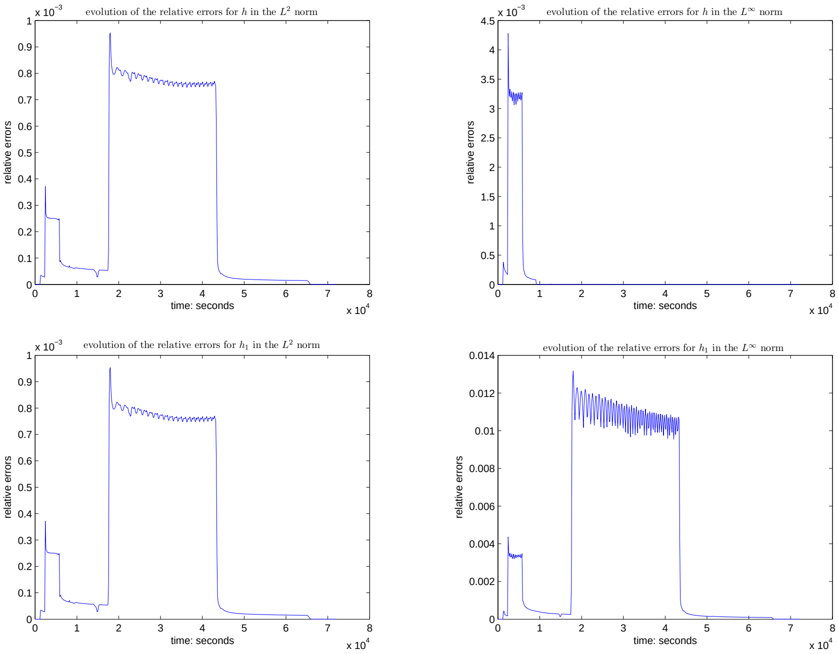

Figure 22: The evolution of the relative errors for the free surfaces h (on the top) and h_1 (on the bottom) in the case of $\epsilon=-0.2$ (L^2 and L^∞ norms).

We use a finite volume method to solve this system of equations, and to be specific we use the central-upwind scheme; see [1].

The equations and all quantities being non-dimensional, we consider the flow in the domain

$$\mathcal{M} = (-24,24) \times (-8,8),$$

over the interval of time $0 < t < T$. We have:

$$\begin{cases} \dfrac{\partial h}{\partial t} + \dfrac{\partial uh}{\partial x} + \dfrac{\partial vh}{\partial y} = 0, \\ \dfrac{\partial uh}{\partial t} + \dfrac{\partial hu^2}{\partial x} + \dfrac{\partial huv}{\partial y} + \dfrac{g}{2}\dfrac{\partial h^2}{\partial x} - fvh = 0, \\ \dfrac{\partial vh}{\partial t} + \dfrac{\partial huv}{\partial x} + \dfrac{\partial hv^2}{\partial y} + \dfrac{g}{2}\dfrac{\partial h^2}{\partial y} + fuh = 0. \end{cases} \tag{3.1}$$

In (3.1), we have the following unknowns and constants:

- h is the fluid depth above the bottom which is supposed flat;
- u and v are the x and y components of the velocity;
- g denotes the gravity, in this case $g = 1$;
- f is the Coriolis force, which is equal to $f_0 + \bar{f}y$, in this case $f_0 = 0$ and $\bar{f} = 1$.

The initial data are the following:

$$\begin{cases} u(x,y,0) = \phi(x)\dfrac{(-9+6y^2)}{4}e^{-\frac{y^2}{2}}, \\ v(x,y,0) = \dfrac{\partial \phi(x)}{\partial x}(2y)e^{-\frac{y^2}{2}}, \\ h(x,y,0) = \phi(x)\dfrac{(3+6y^2)}{4}e^{-\frac{y^2}{2}} + 1, \end{cases} \tag{3.2}$$

with:

$$B = 0.395, \quad A = 0.7771B^2, \quad \phi(x) = A\,\mathrm{sech}^2 Bx,$$
$$\frac{\partial \phi(x)}{\partial x} = -2B\tanh(Bx)\phi.$$

The Dirichlet boundary conditions read:

$$h_{\partial\mathcal{M}} = 1, \qquad u_{\partial\mathcal{M}} = 0, \qquad v_{\partial\mathcal{M}} = 0. \tag{3.3}$$

The Neumann boundary conditions simply read:

$$\frac{\partial h}{\partial n} = \frac{\partial u}{\partial n} = \frac{\partial v}{\partial n} = 0, \quad \text{on } \partial\mathcal{M}. \tag{3.4}$$

For the transparent boundary conditions we have two different sets of boundary conditions, one boundary condition for the North and East boundaries and two boundary conditions for the West and South boundaries. These boundary conditions are not applied on the unknowns h, u, v but, as in the 1D case, on suitable combinations defined as follows:

$$\text{West, East}\left\{\begin{aligned}\alpha^{WE}&=\frac{u}{2}-\sqrt{gh},\\ \beta^{WE}&=v,\\ \gamma^{WE}&=\frac{u}{2}+\sqrt{gh},\end{aligned}\right. \qquad \text{North, South}\left\{\begin{aligned}\alpha^{NS}&=\frac{v}{2}-\sqrt{gh},\\ \beta^{NS}&=u,\\ \gamma^{NS}&=\frac{v}{2}+\sqrt{gh}.\end{aligned}\right. \tag{3.5}$$

With these variables the transparent boundary conditions that we propose are, for the North and East boundaries, Dirichlet boundary conditions for α^{NS} and α^{WE}. These conditions hence read:

- North boundary:

$$\alpha^{NS}=\alpha^{NS}_{\partial\mathcal{M}}, \tag{3.6}$$

- East boundary:

$$\alpha^{WE}=\alpha^{WE}_{\partial\mathcal{M}}, \tag{3.7}$$

where $\alpha^{WE}_{\partial\mathcal{M}}=u_{\partial\mathcal{M}}/2-\sqrt{gh_{\partial\mathcal{M}}}$, $\alpha^{NS}_{\partial\mathcal{M}}=v_{\partial\mathcal{M}}/2-\sqrt{gh_{\partial\mathcal{M}}}$ and $h_{\partial\mathcal{M}}$, $u_{\partial\mathcal{M}}$, $v_{\partial\mathcal{M}}$ are defined in (3.3).

For the West and South boundaries we use a Dirichlet boundary condition for α^{NS}, α^{WE}, β^{NS} and β^{WE}. Hence:

- West boundary:

$$\left\{\begin{aligned}\beta^{WE}&=\beta^{WE}_{\partial\mathcal{M}},\\ \gamma^{WE}&=\gamma^{WE}_{\partial\mathcal{M}},\end{aligned}\right. \tag{3.8}$$

- South boundary:

$$\left\{\begin{aligned}\beta^{NS}&=\beta^{NS}_{\partial\mathcal{M}},\\ \gamma^{NS}&=\gamma^{NS}_{\partial\mathcal{M}},\end{aligned}\right. \tag{3.9}$$

where $\gamma^{WE}_{\partial\mathcal{M}}=u_{\partial\mathcal{M}}/2+\sqrt{gh_{\partial\mathcal{M}}}$, $\gamma^{NS}_{\partial\mathcal{M}}=v_{\partial\mathcal{M}}/2+\sqrt{gh_{\partial\mathcal{M}}}$, $\beta^{NS}_{\partial\mathcal{M}}=u_{\partial\mathcal{M}}$, $\beta^{WE}_{\partial\mathcal{M}}=v_{\partial\mathcal{M}}$ and $h_{\partial\mathcal{M}}$, $u_{\partial\mathcal{M}}$ and $v_{\partial\mathcal{M}}$ are defined in (3.3). Once we know α, β and γ on the boundary (or on a fictitious cell) we can then find the values of our unknowns h, u, v by inverting the system (3.5).

Besides these boundary conditions which are based on an ongoing theoretical work using the Kreiss-Lopatinsky condition [15], our numerical code remains underdetermined, and we resolved this difficulty by imposing the same boundary values at two contiguous boundary points which amounts to imposing a Neumann boundary condition; this was done for β and γ on the north and east boundaries, and for α on the west and south boundaries.

3.1 Numerical procedure

Before explaining how we incorporate these boundary conditions we explain our numerical scheme. We first rewrite the system in the conservative form which reads

$$\frac{\partial Q}{\partial t}+\frac{\partial F(Q)}{\partial x}+\frac{\partial G(Q)}{\partial y}=S, \tag{3.10}$$

where $U=uh$, $V=vh$ and

$$Q=\begin{pmatrix} h \\ U \\ V \end{pmatrix}, \quad F(Q)=\begin{pmatrix} U \\ \frac{U^2}{h}+\frac{gh^2}{2} \\ \frac{UV}{h} \end{pmatrix}, \quad G(Q)=\begin{pmatrix} V \\ \frac{UV}{h} \\ \frac{V^2}{h}+\frac{gh^2}{2} \end{pmatrix}. \tag{3.11}$$

The discretization of the domain $\mathcal{M}$ is done using rectangular finite volumes $K_m=[x_{m/w},x_{m/e}]\times[y_{m/s},y_{m/n}]$ of centers (x_m,y_m), and of size $\Delta x\times\Delta y$, where N_x, N_y are two integers such that $N_x\Delta x=L_x$ and $N_y\Delta y=L_y$.

The unknowns will be approximations of the cell averages:

$$Q_m(t)=\frac{1}{\Delta x\Delta y}\int_{K_m}Q(t,x,y)dxdy,$$

where $Q_m(t)=(h_m(t),U_m(t),V_m(t))^T$.

In order to obtain the discretized equations, we integrate the system (3.10) on each cell K_m and we divide by its area $\Delta x\Delta y$; we find

$$\frac{d}{dt}Q_m(t)=-\frac{H^x_{m/e}(t)-H^x_{w/m}(t)}{\Delta x}-\frac{H^y_{m/n}(t)-H^y_{s/m}(t)}{\Delta y}. \tag{3.12}$$

The fluxes $H^x_{m/e}(t)$ and $H^y_{m/n}(t)$ are respectively the east flux (along the x-axis) and the north flux (along the y-axis) on the edges between K_m and K_e, and between K_m and K_n, see Fig. 23. The other fluxes are defined similarly.

We write one of the fluxes explicitly:

$$H^x_{m/e}(t)=\frac{1}{\Delta x}\int_{\Gamma_{m/e}}F(Q(t,x,y))dy.$$

The approximation of the fluxes is done using a semi-discrete central-upwind scheme (as in [18,19]); that is

$$H^x_{m/e}\cong\frac{a^+_{m/e}F(Q^E_m)-a^-_{m/e}F(Q^W_e)}{a^+_{m/e}-a^-_{m/e}}+\frac{a^+_{m/e}a^-_{m/e}(Q^W_e-Q^E_m)}{a^+_{m/e}-a^-_{m/e}}, \tag{3.13}$$

$$H^y_{m/n}\cong\frac{b^+_{m/n}G(Q^N_m)-b^-_{m/n}G(Q^S_n)}{b^+_{m/n}-b^-_{m/n}}+\frac{b^+_{m/n}b^-_{m/n}(Q^S_n-Q^N_m)}{b^+_{m/n}-b^-_{m/n}}, \tag{3.14}$$

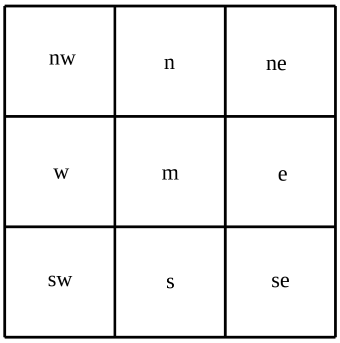

Figure 23: The NSWE stencil.

with the following one-sided local speeds of propagation:

$$a^+_{m/e}=\max\left[\lambda_{\max}\left(\frac{\partial F}{\partial Q}(Q^W_e)\right),\lambda_{\max}\left(\frac{\partial F}{\partial Q}(Q^E_m)\right),0\right], \tag{3.15a}$$

$$b^+_{m/n}=\max\left[\lambda_{\max}\left(\frac{\partial G}{\partial Q}(Q^S_n)\right),\lambda_{\max}\left(\frac{\partial G}{\partial Q}(Q^N_m)\right),0\right], \tag{3.15b}$$

$$b^-_{m/n}=\min\left[\lambda_{\min}\left(\frac{\partial G}{\partial Q}(Q^S_n)\right),\lambda_{\min}\left(\frac{\partial G}{\partial Q}(Q^N_m)\right),0\right]. \tag{3.15c}$$

Here $\lambda_{\max}(\frac{\partial F}{\partial Q}(\tilde{Q}))$ and $\lambda_{\min}(\frac{\partial F}{\partial Q}(\tilde{Q}))$ (resp. $\lambda_{\max}(\frac{\partial G}{\partial Q}(\tilde{Q}))$ and $\lambda_{\min}(\frac{\partial G}{\partial Q}(\tilde{W}))$) are respectively the largest and the smallest eigenvalues of the Jacobian matrix of F, $\frac{\partial F}{\partial Q}$ (resp. of G, $\frac{\partial G}{\partial Q}$) at the point $\tilde{Q}$.

To compute the values Q^E_m, Q^W_m, Q^N_m, Q^S_m we use a non-oscillatory linear polynomial to evaluate the value of Q at these points:

$$Q^E_m=p_m(t,x_{m/e},y_m),\qquad Q^W_m=p_m(t,x_{m/w},y_m),$$
$$Q^N_m=p_m(t,x_m,y_{m/n}),\qquad Q^S_m=p_m(t,x_m,y_{m/s}),$$

where $p_m(t,x_m,y_m)=Q_m(t)+s^x_m(t)(x-x_m)+s^y_m(t)(y-y_m)$.

The same method is used for the reconstruction on the cells K_e, K_w, K_n and K_s. For the polynomial of reconstruction we use a minmod (see (2.15)) slope in order to obtain a second order scheme. The slopes are the following:

$$s^x_m(t)=\text{minmod}\left(\theta\frac{Q_m(t)-Q_w(t)}{\Delta x};\frac{Q_e(t)-Q_w(t)}{2\Delta x};\theta\frac{Q_e(t)-Q_m(t)}{\Delta x}\right), \tag{3.16a}$$

$$s^y_m(t)=\text{minmod}\left(\theta\frac{Q_m(t)-Q_s(t)}{\Delta y};\frac{Q_n(t)-Q_s(t)}{2\Delta y};\theta\frac{Q_n(t)-Q_m(t)}{\Delta y}\right), \tag{3.16b}$$

where $\theta\in[1,2]$.

The parameter $\theta\in[1,2]$ is chosen in an empirical optimal way in order to obtain good results; we usually take θ to be equal to 1.6.

The definitions above of the fluxes are valid for the volumes inside $\mathcal{M}$. For the cells at the boundary of our mesh, we create fictitious cells in the case of Neumann and transparent boundary conditions. With the Neumann boundary conditions the value outside the domain the same as the one inside the domain, as for transparent boundary conditions the value of h, U and V are computed using the unknowns α, β, γ.

In the case of the Dirichlet boundary conditions we have

- If "**n**" does not exist:
$$H^y_{m/n}=G(Q^N_{\partial\mathcal{M}});$$
- If "**s**" does not exist:
$$H^y_{s/m}=G(Q^S_{\partial\mathcal{M}});$$
- If "**e**" does not exist:
$$H^x_{m/e}=F(Q^E_{\partial\mathcal{M}});$$
- If "**w**" does not exist:
$$H^x_{w/m}=F(Q^W_{\partial\mathcal{M}}),$$

with

$$\begin{aligned}
&h^N_{\partial\mathcal{M}}=h^S_{\partial\mathcal{M}}=h^E_{\partial\mathcal{M}}=h^W_{\partial\mathcal{M}}=h_{\partial\mathcal{M}}=1,\\
&U^N_{\partial\mathcal{M}}=U^S_{\partial\mathcal{M}}=U^E_{\partial\mathcal{M}}=U^W_{\partial\mathcal{M}}=U_{\partial\mathcal{M}}=0,\\
&V^N_{\partial\mathcal{M}}=V^S_{\partial\mathcal{M}}=V^E_{\partial\mathcal{M}}=V^W_{\partial\mathcal{M}}=V_{\partial\mathcal{M}}=0.
\end{aligned}$$

The space scheme being now defined, we introduce our time scheme namely, a fourth order Runge-Kutta method. Let $T>0$ be fixed; denote the time step by $\Delta t=T/N_{it}$, where N_{it} is an integer representing the total number of time iterations; for $n=0,\cdots,N_{it}$ we define Q^n as the approximate value of Q at time $t_n=n\Delta t$.

We rewrite (3.12) as
$$\frac{d}{dt}Q_m=R(Q_m(t),t),$$
and the Runge-Kutta scheme of order 4 reads:

$$\left\{\begin{aligned}
&k^n_{1,m}=R(Q^n_m,t_n),\\
&k^n_{2,m}=R(Q^n_m+\tfrac{\Delta t}{2}k^n_{1,m},t_n+\tfrac{\Delta t}{2}),\\
&k^n_{3,m}=R(Q^n_m+\tfrac{\Delta t}{2}k^n_{2,m},t_n+\tfrac{\Delta t}{2}),\\
&k^n_{4,m}=R(Q^n_m+\Delta t k^n_{3,m},t_n+\Delta t),\\
&Q^{n+1}_m=Q^n_m+\tfrac{\Delta t}{6}(k^n_{1,m}+2k^n_{2,m}+2k^n_{3,m}+k^n_{4,m}).
\end{aligned}\right. \tag{3.17}$$

3.2 Numerical results

Since the soliton travels from the West to the East, we only apply the Neumann or transparent boundary conditions on the West and East boundaries. We always use the Dirichlet boundary conditions on the North and South boundaries. There is no activity on the North and South boundaries therefore the conditions on these boundary do not affect the computation. Below we say Neumann boundary conditions when we apply Neumann on the West and East boundaries and Dirichlet on the North and South boundaries; we say transparent boundary conditions when we apply the transparent conditions on the West and East boundaries and Dirichlet on the North and South boundaries.

The results of the numerical simulations are displayed in Figs. 24, 25 and 26 for the Neumann boundary conditions in the left columns, and for the transparent conditions

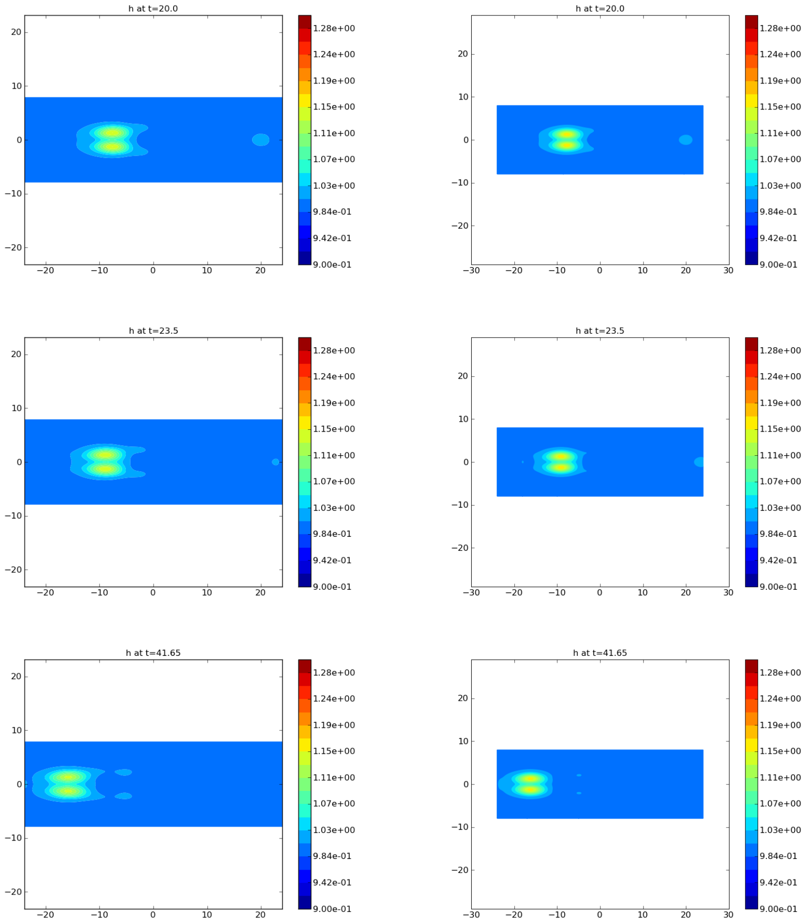

Figure 24: Evolution of the Rossby soliton at the indicated times (20, 23.5, 41.65). Left column: Neumann boundary condition; right column: transparent boundary condition.

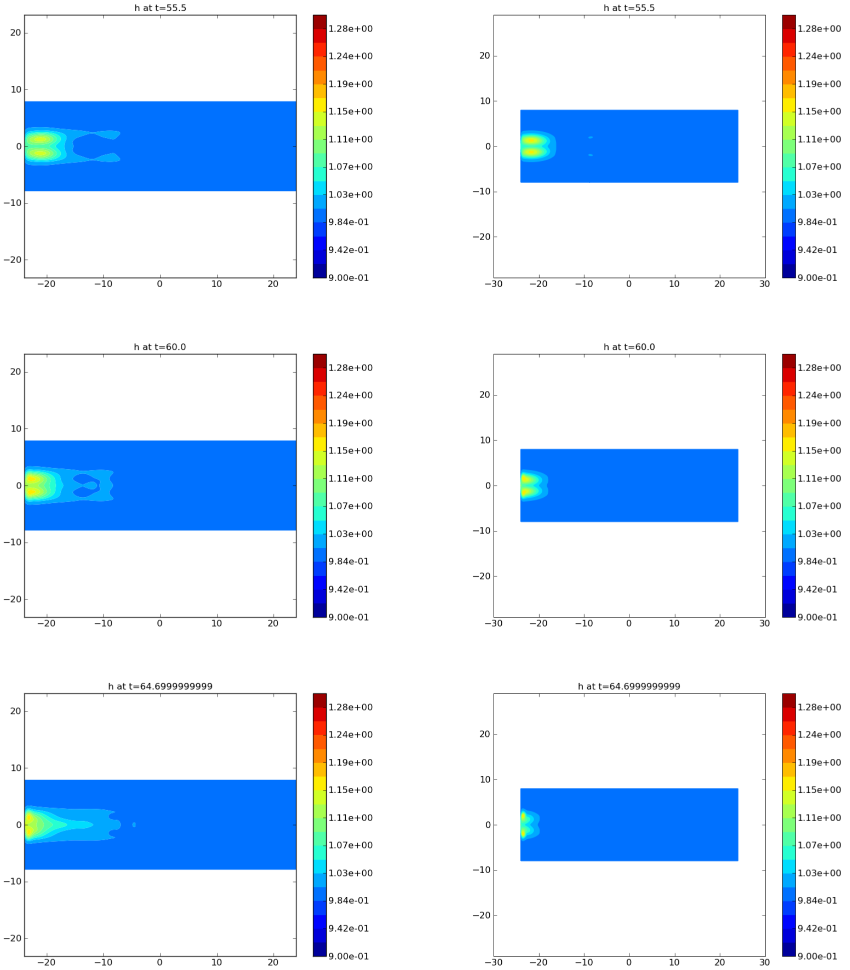

Figure 25: Evolution of the Rossby soliton at the indicated times (55.5, 60, 64.7). Left column: Neumann boundary condition; right column: transparent boundary condition.

in the right columns. As expected, the behavior of the soliton is essentially the same in both cases until the soliton reaches the boundary at time $t=41.65$. Then the behaviors are different with a reflection of the waves appearing at both the left and right boundaries ($x=\pm 24$) for the Neumann boundary condition. Note, at time $t=64.69$, the important reflected wave on the left while in the right column the soliton leaves the domain without reflexion at all. On the contrary, in the right column the soliton continues to leave smoothly the domain until it has completely disappeared at time $t=300$. Eventually the soliton leaves the domain in the case of Neumann boundary conditions, at a time slightly higher than with transparent boundary conditions.

Fig. 27 shows that after $t\simeq 65$, the calculations with the Dirichlet condition are not

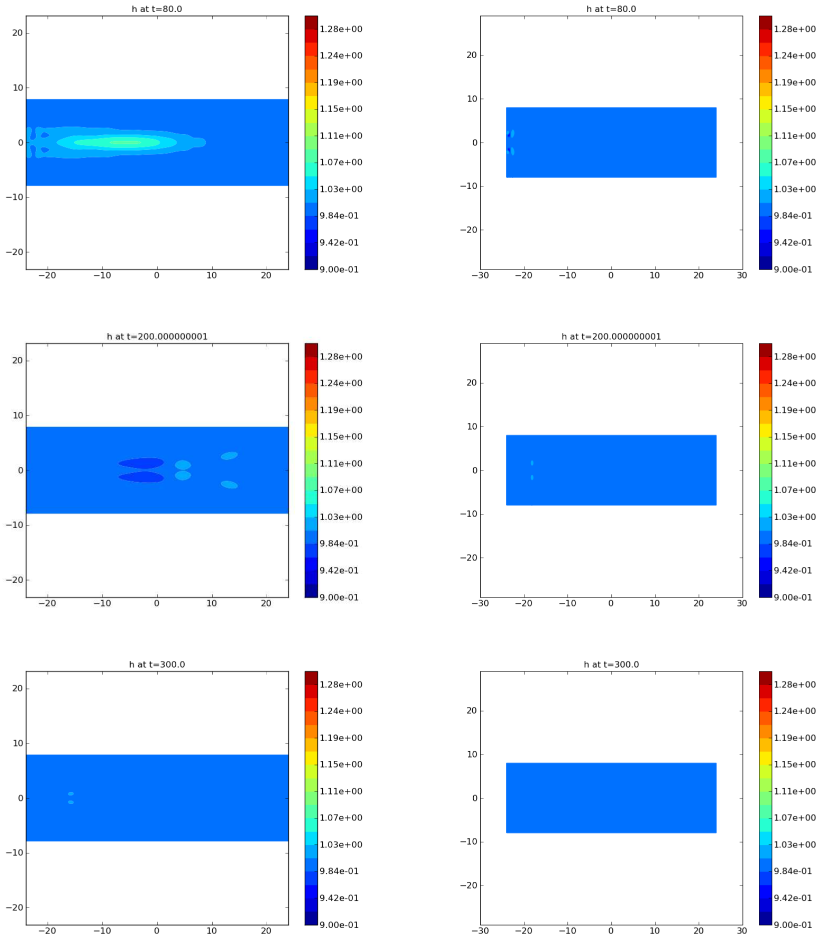

Figure 26: Evolution of the Rossby soliton at the indicated times (80, 200, 300). Left column: Neumann boundary condition; right column: transparent boundary condition.

valid anymore, giving an indication that the solution blows up, and that the shallow water equations are not well posed with the Dirichlet boundary conditions (3.3).

We also verify our boundary conditions with a soliton coming in our domain from the west. We first did a computation on a larger domain in x, $(x,y)\in(-72,72)\times(-8,8)$, and we saved the values. From these values we computed the boundary values of α, β, γ on the smaller domain $(x,y)\in(-24,24)\times(-8,8)$, with the same mesh as the larger domain. The boundary conditions for α, β, γ are the same as described before, it is just the values of h, u and v that differ. Fig. 28 shows our results, we can see that the soliton comes in nicely and exits the same way as in our previous computations. We can remark that the soliton is more stretched but this comes from the fact that our domain for the initial data and boundary values for the soliton was three times larger in x.

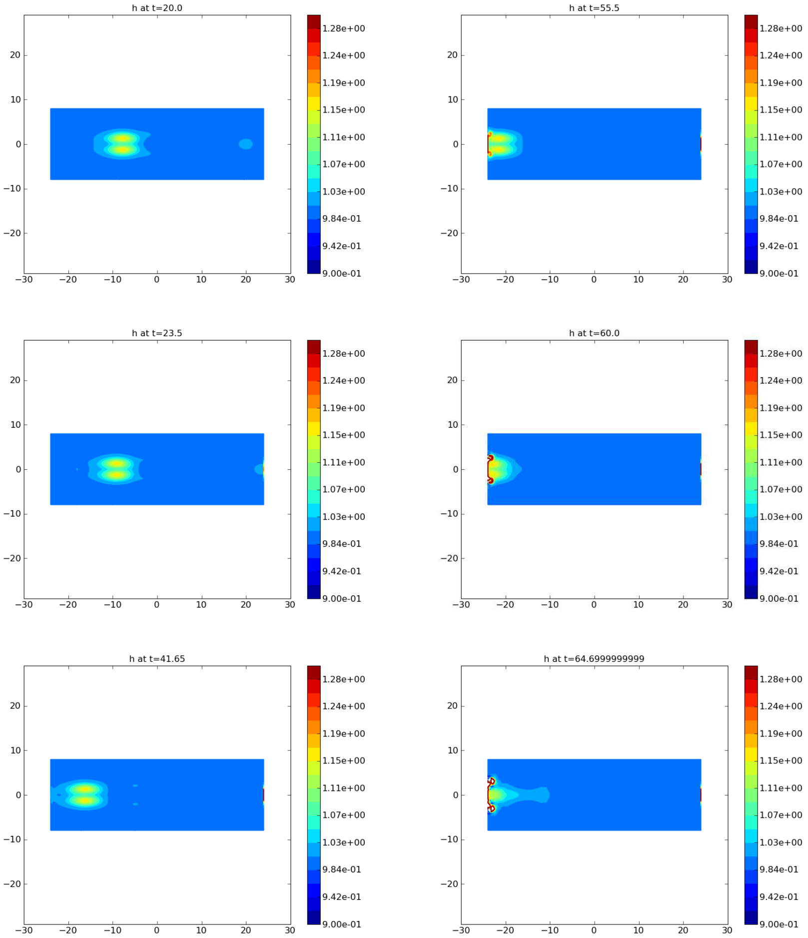

Figure 27: Evolution of the Rossby soliton at the indicated times (20, 23.5, 41.65, 55.5, 60, 64.7), with the Dirichlet boundary conditions.

Finally we compare the values on the smaller domain $-24<x<24$, that we obtain from these two different calculations: calculation on the larger domain $-72<x<72$ (considered as the reference calculation), restricted to $-24<x<24$, and the calculation on the small domain $-24<x<24$ using the boundary values from the large domain calculation and the boundary condition previously described. Fig. 29 shows that the corresponding error is of order $10^{-3}\sim 10^{-4}$.

Fig. 30 shows the energy computed with the Dirichlet boundary conditions, on the left, and with the transparent boundary conditions on the right. In the case of the Dirichlet boundary conditions the energy blows up as soon as the soliton hits the west boundary. As for the transparent boundary conditions, the energy stays relatively constant, which is expected. Fig. 31 shows the fluxes on each of the four boundaries of the domain

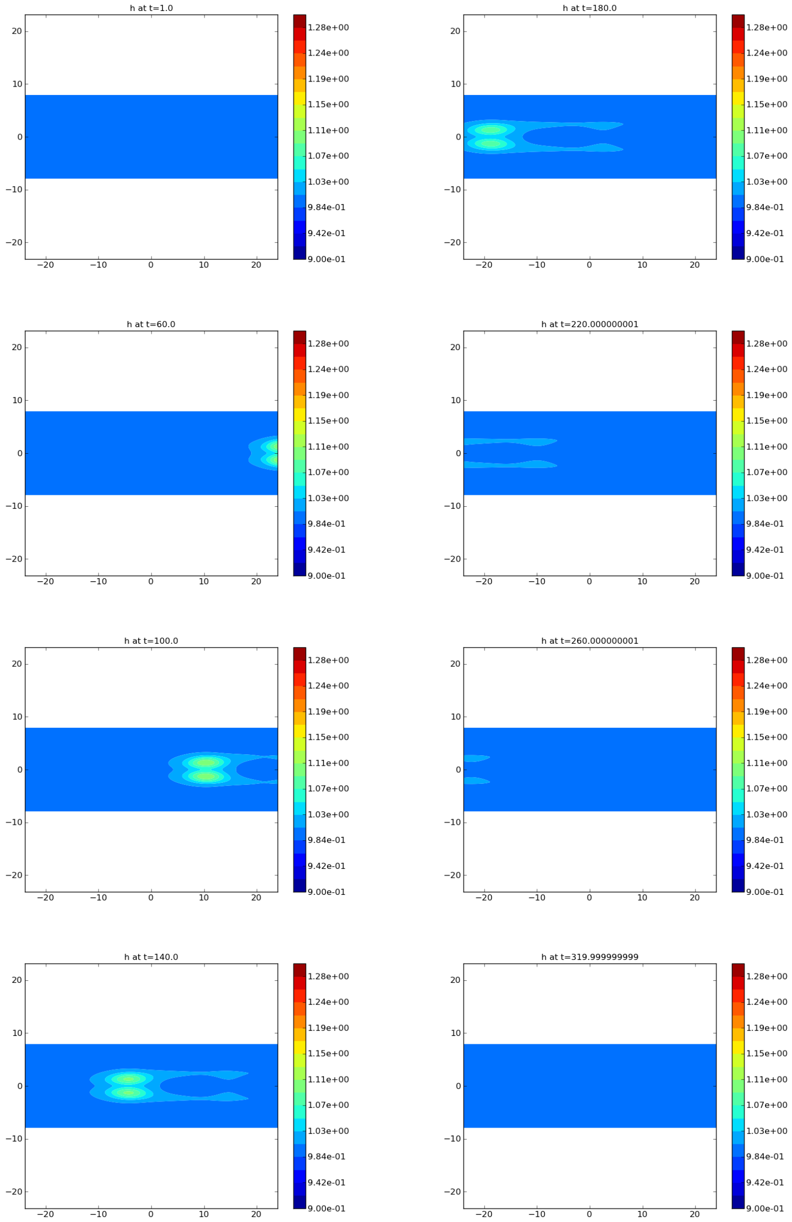

Figure 28: Evolution of the Rossby soliton at the indicated times, using the values for the boundary conditions and initial data from a computation on a larger domain in x, $x \in (-72,72)$ (using the transparent boundary conditions on the smaller domain).

that are computed in the case of transparent boundary conditions. All calculations confirm, in the transparent case, that the flow tends to a stationary solution with no boundary fluxes.

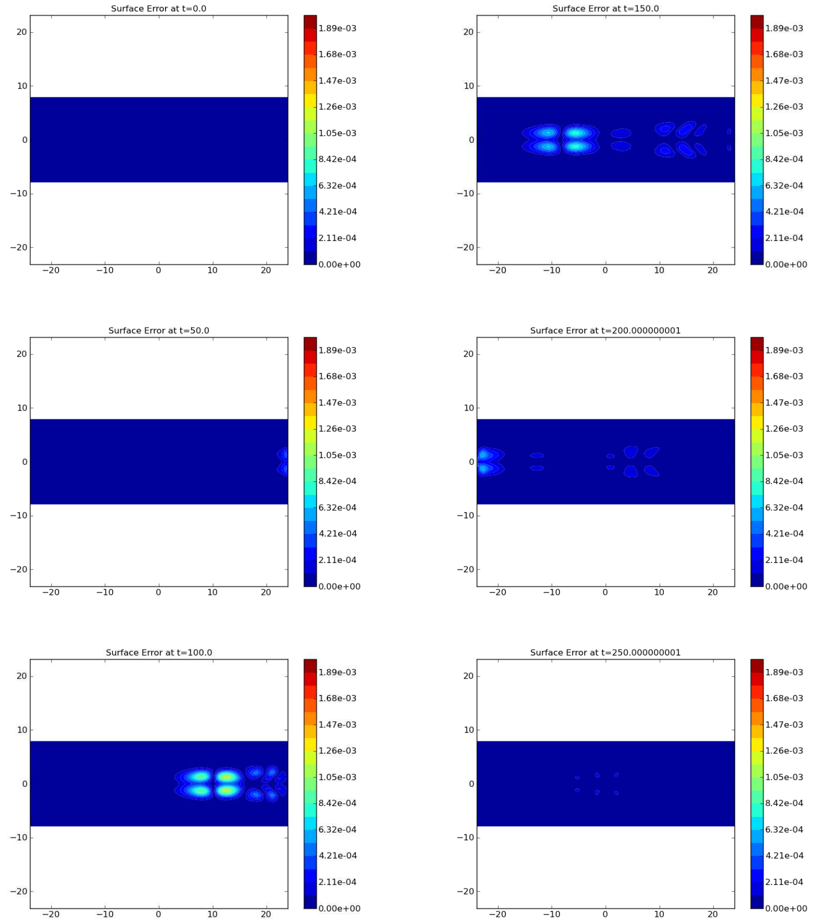

Figure 29: The surface error between the computation on the smaller domain, $(x,y)\in(-24,24)\times(-8,8)$, and that on the larger domain $(x,y)\in(-72,72)\times(-8,8)$.

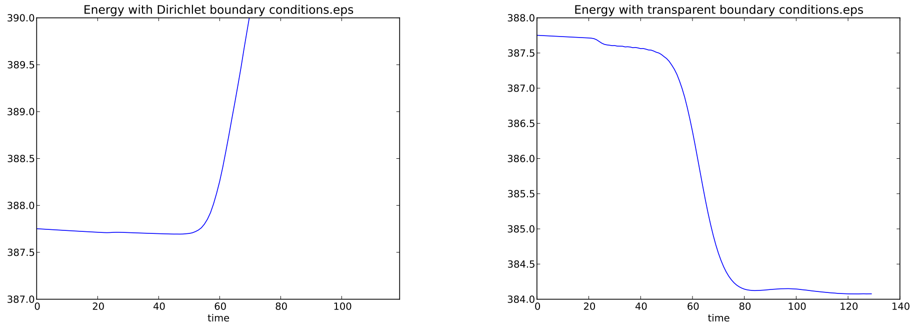

Figure 30: On the left the energy of the soliton with Dirichlet boundary conditions and on the right the energy of the soliton with transparent boundary conditions. Note the blow up with the Dirichlet boundary conditions.

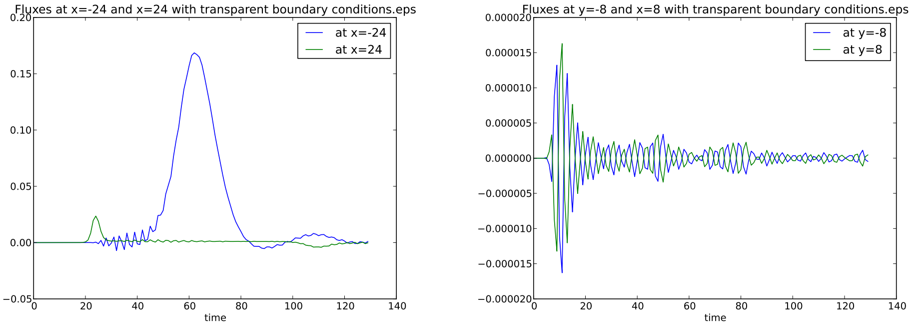

Figure 31: On the left the fluxes on the west and east boundaries and on the right the fluxes on the south and north boundaries, using transparent boundary conditions.

Remark 3.1. As in Remark 2.2, we observe that, to the best of our knowledge, this is the only article treating a 2 D shallow water model without any artificial numerical viscosity; e.g. in the related article [22], the authors propose and implement a sponge method which consists in adding some artificial viscosity near the boundary.

4 Conclusion

New boundary conditions have been proposed for the inviscid shallow water equations in space dimension one and two. Fully (in 1D) or partly (in 2D) supported by theoretical studies, these boundary conditions are shown to be ”transparent”, to some extent (to the precision of the figures), in our numerical simulations, that is they let the waves move freely in and out of the domain. The numerical tests include two layers of fluid in space dimension one and one layer of fluid in space dimension two in a rectangle, a case related to the classical equatorial Rossby soliton. Without any attempt at systematic comparison with other open boundary conditions, it is observed that the classical equatorial Rossby soliton with Dirichlet or Neumann boundary conditions leads to undesirable reflexions when the soliton reaches the boundary, and eventually to numerical blow-up in the case of the Dirichlet condition. In the case of the Neumann boundary condition, substantial reflexions occur at the boundary but the calculation does not blow up and the soliton eventually leaves the domain. Finally for the proposed boundary conditions the soliton moves freely in and out of the domain. On the purely computational side, the algorithms that we developed and implemented are purely inviscid, whereas all related earlier works that we are aware of introduced some sort of viscosity.

Acknowledgments

This work was supported in part by the NSF Grant DMS 0906440 and DMS 1206438, and by the Research Fund of Indiana University. Ming-Cheng Shiue was also partially supported by the National Science Council of Taiwan under research grants NSC-100-2115-M-009-009-MY2.

References

[1] K. Adamy, A. Bousquet, S. Faure, J. Laminie and R. Temam, A multilevel method for finite volume discretization of the two-dimensional nonlinear shallow-water equations, Ocean Modelling, vol. 33 (2010), Issues 3-4, 235-256.

[2] R. Abgrall and S. Karni, Two-layer shallow water system: a relaxation approach, SIAM J. Sci. Comput., vol. 31 (2009), no. 3, 1603-1627.

[3] E. Audusse, A multilayer Saint-Venant System: Derivation and Numerical Validation, Discrete Contin. Dyn. Syst. Ser. B, vol.5 (2005), 189–214.

[4] P.G. Baines, 1998, Topographic effects in stratified flows, Cambridge Univ. Press, Cambridge, U. K., 1998.

[5] A.F. Bennett and B. S. Chua, Open boundary conditions for Lagrangian geophysical fluid dynamics, J. Comput. Phys., vol. 153 (1999), no. 2, 418-436.

[6] E. Blayo and DL. ebreu, Revisiting open boundary conditions from the point of view of characteristic variables, Ocean Modelling, vol. 9 (2005), 231–252.

[7] A. F. Bennett and P.E. Kloeden, Boundary conditions for limited-area forecasts, J. Atmospheric Sci., vol. 35 (1978), no. 6, 990-996.

[8] S. Benzoni-Gavage and D. Serre, Multidimensional hyperbolic partial differential equations,First-order systems and applications. Oxford Mathematical Monographs, The Clarendon Press, Oxford University Press, Oxford, 2007.

[9] F. Bouchut and V. Zeitlin, A robust well-balanced scheme for multi-layer shallow water equations, DCDS-B, vol. 13 (2010), no. 4, 739–758.

[10] M.J.P. Cullen, Analysis of the semi-geostrophic shallow water equations, Phys. D, vol. 237 (2008), 1461-1465.

[11] B. Engquist and L. Halpern, Far field boundary conditions for computation over long time, Appl. Numer. Math., vol. 4 (1988), no. 1, 21-45.

[12] B. Engquist and A. Majda, Absorbing boundary conditions for the numerical simulation of waves, Math. Comp. 31 (1977), no. 139, 629-651.

[13] W. W. Grabowski, Coupling cloud processes with large-scale dynamics using the cloud-resolving convection parameterization (CRCP), J. Atmospheric Sciences, Vol 58 (2001), 978V997

[14] L. Halpern and J. Rauch, Absorbing boundary conditions for diffusion equations, Numer. Math., vol. 71 (1995), no. 2, 185-224.

[15] A. Huang, M. Petcu and R. Temam, The nonlinear 2d supercritical inviscid shallow water equations in a rectangle, in preparation (under completion).

[16] A. Huang and R. Temam, The linearized 2d inviscid shallow water equations in a rectangle: boundary conditions and well-posedness, submitted, arXiv:1209.3194.

[17] A. Huang and R. Temam, The nonlinear 2d subcritical inviscid shallow water equations with periodicity in one direction, in preparation (under completion).

[18] A. Kurganov, S. Noelle and G. Petrova, Semi-discrete central upwind schemes for hyperbolic conservation laws and Hamilton-Jacobi equations, SIAM J. Sci. Comput., vol. 23(2001), no. 3, 707-740.

[19] A. Kurganov and G. Petrova, Central-upwind schemes for the Saint-Venant system, Math. Modell. Numer. Anal., vol. 34(2000), 1259-1275.

[20] H.-O. Kreiss, Initial boundary value problems for hyperbolic systems, Comm. Pure Appl. Math., vol. 23 (1970), 277-298.

[21] Ya. B. Lopatinsky, The mixed Cauchy-Dirichlet type problem for equations of hyperbolic type, Dopovfdf Akad. Nauk Ukrain. RSR Ser. A, vol. 668 (1970), 592-594.

[22] J.W. Lavelle and W.C. Thacker, A pretty good sponge: Dealing with open boundaries in limited-area ocean models, Ocean Modelling, vol. 20 (2008), no. 3, 270-292.

[23] T.-T. Li and W.-C. Yu, Boundary value problems for quasilinear hyperbolic systems,Duke University Mathematics Series, V. Duke University, Mathematics Department, Durham, NC, 1985

[24] A. McDonald, Transparent boundary conditions for the shallow water equations: testing in a nested environment, Mon. Wea. Rev., vol. 131 (2003), 698-705.

[25] J. Nycander, A. McC. Hogg and L. M. Frankcombe, Open boundary conditions for nonlinear channel flow, Ocean Modelling, vol. 24 (2008), 108-121.

[26] I. M. Navon, B. Neta and M. Y. Hussaini, A perfectly matched layer approach to the linearized shallow water equations models, Monthly Weather Review, vol. 132 (2004), 1369-1378.

[27] J. Oliger and A. Sundstrom, Theoretical and practical aspects of some initial boundary value problems in fluid dynamics, SIAM J. Appl. Math., vol. 35 (1978), 419-446.

[28] E. Palma and R. Matano, On the implementation of passive open boundary conditions for a general circulation model: The barotropic mode, J. of Geophysical Research, vol 103 (1998), 1319-1341.

[29] M. Petcu and R. Temam, The one-dimensional shallow-water equations with transparent boundary conditions, Mathematical Methods in the Applied Sciences, (MMAS)(2011); DOI: 10; 1002/mma, 1482.

[30] M. Petcu and R. Temam, An interface problem: the two-layer shallow water equations, DCDS-A, 2011, to appear.

[31] D. Randall, M. Khairoutdinov, A. Arakawa and W. Grabowski, Breaking the cloud parameterization deadlock, Bulletin of the American Meteor. Society (BAMS) (2003), 1547-1564, DOI: 10.1175/BAMS-84-11-1547

[32] A. Rousseau, R. Temam and J. Tribbia, Boundary value problems for the inviscid primitive equations in limited domains, in Computational Methods for the Oceans and the Atmosphere, Special Volume of the Handbook of Numerical Analysis, P. G. Ciarlet, Ed, Temam, R. and Tribbia, J., Guest Eds, Elesevier, Amsterdam (2009), 377-385.

[33] R. Salmon, Numerical solution of the two-layer shallow water equation with bottom topography, Journal of Marine Research, vol. 60 (2002), 605-638.

[34] M.-C. Shiue, J. Laminie, R. Temam and J. Tribbia, Boundary value problems for the shallow water equations with topography, J. Geophy. Res., vol. 116 (2011), C02015.

[35] R. Temam and J. Tribbia, Open boundary conditions for the primitive and Boussinesq equations, J. Atmospheric Sci., vol. 60 (2003), 2647-2660.

[36] A.M. Treguier, B. Barnier, A.P. de Miranda, J.M. Molines, N. Grima, M. Imbard, G. Madec, C. Messager, T. Reynald and S. Michel, An eddy-permitting model of the Atlantic circulation: evaluating open boundary conditions. J. Geophys, Res. 106 (2001), 22115V22129.

[37] B. Whitham, Linear and nonlinear waves, Pure and Applied Mathematics (New York). A Wiley-Interscience Publication. John Wiley & Sons, Inc., New York, 1999.

[38] T. Warner, R. Peterson and R. Treadon, A tutorial on lateral boundary conditions as a basic and potentially serious limitation to regional numerical weather prediction, Bull. Amer. Meteor. Soc., vol. 78(1997), 2599-2617.